

1 **QUARTZ TEXTURAL ANALYSIS FROM AN ANASTOMOSING SHEAR**
2 **ZONE SYSTEM: IMPLICATIONS FOR THE TECTONIC EVOLUTION OF**
3 **THE RIBEIRA BELT, BRAZIL**

4
5 T. Conte¹, C. Cavalcante^{1,2}, L.E. Lagoeiro¹, H. Fossen³, C.S. Silveira¹

6
7 ¹UFPR – Federal University of Paraná, Department of Geology, Av. Cel. Francisco
8 Heráclito dos Santos, 100, 81531-980 Curitiba, PR, Brazil.

9 ²UiT – University of Tromsø, The Arctic University of Norway, Department of
10 Geosciences, Dramsveien 201, 9037 Tromsø, Norway.

11 ³UiB – University of Bergen, Museum of Natural History, Allégaten 41, 5007 Bergen,
12 Norway.

13
14
15 **ABSTRACT**

16
17 Strain localization and influence of grain-size reduction processes were investigated
18 from field and microstructural observations, and from quartz textural analysis using
19 EBSD, in rocks deformed along an anastomosing network of shear zones in the Ribeira
20 belt in Brazil. Rocks deformed along the Lancinha shear zone (LSZ) display high
21 percentage of recrystallized grains, in which quartz recrystallized grain size from rocks
22 in the southern LSZ reaches a maximum of 50 μm , and in the northern LSZ a maximum
23 of 200 μm . The dominant serrated grain boundaries and the widespread (50-85%)
24 presence of very small (>10-50 μm) recrystallized quartz grains, suggest that BLG was
25 the dominant recrystallization mechanism responsible for grain-size reduction in the
26 south portion of the LSZ. In the northern LSZ the presence of large recrystallized grains
27 with sizes close to subgrains, suggests that grain-size reduction occurred by SGR, and
28 the presence of lobate grain boundaries point to GBM recrystallization, which led to an
29 increase in recrystallized grain size. This suggests grain-size reduction by dynamic
30 recrystallization as a major factor leading to weakening and strain localization.
31 Evidence of intracrystalline deformation and the well-developed quartz crystallographic
32 fabrics suggest that strain localization in the LSZ occurred by dislocation creep
33 deformation mechanisms. Dislocation creep is recorded by dominant activation of basal
34 <a> slip and secondary contribution of rhomb <a> slip, in the southeast of the LSZ, and
35 by activation of rhomb <a> + basal <a> and prism <a> in the northeast. These slip
36 systems together with microstructural observations suggest that plastic deformation
37 occurred at around 400 °C in the southern region, and at around at >400 to 500 °C in the
38 northern region. S-C foliation, quartz <c> axis distribution and several kinematic
39 indicators suggest sinistral sense of shear along the LSZ, and strain partitioning during
40 progressive deformation. The dominance of sinistral indicators observed in the LSZ are
41 also found in parallel shear zones to the east, such as the Putunã and Serra do Azeite.
42 The sinistral kinematics in this overall dextral transpressional orogenic system may be
43 explained by dual sense of shear on shear zones bounding extruding blocks, likely
44 formed during progressive orogenic evolution instead of the polyphase evolution
45 previously suggested for this southern part of the Ribeira belt.

46

1. INTRODUCTION

Shear zones are known as narrow zones that localize lithospheric deformation (Ramsay, 1980). Anastomosing shear zone systems represent mature stages of development that often record long progressive deformation histories. Many are associated with orogenic belts, such as the >900 km long and ~170 km wide anastomosing shear zone network found in the Ribeira belt that developed from 600 to 520 Ma, during the Brasiliano/Pan-African orogeny (Bento dos Santos et al., 2015; Machado et al., 2016). Exploring such shear zone systems and the way they accommodate deformation is important for our comprehension of crustal rheology and the way crust reacts to plate-scale deformation, and requires investigations at a range of scales and with different techniques.

Rocks in deforming shear zones typically undergo grain-size reduction processes by both brittle and plastic deformation mechanisms, the latter usually involving dynamic recrystallization. In general, such processes decrease the mechanical strength of rocks (Poirier, 1980; Hobbs et al., 1990; Platt and Behr, 2011), resulting in further localization of shear deformation as strain accumulates. Such localization potentially promotes strain partitioning from the microscale to that of an orogenic belt, producing tectonic domains of contrasting structural style, strain and complexity, and is therefore important to understand.

In the southern Ribeira orogenic belt, the Lancinha shear zone (LSZ) may, together with the Cubatão and Além Paraíba-Pádua shear zones, represent a first-order continental shear zone system (e.g. Sadowski, 1991) that involved intense grain-size reduction from upper to lower crustal levels. Even though observations of overprinting relations, porphyroclast inclusion trails and universal-stage quartz c-axis diagrams have been used to define a series of short-lived deformation phases in this shear zone system (e.g. Faleiros et al., 2016), we consider it a result of progressive deformation, typical for large shear zone systems (e.g. Fossen and Cavalcante, 2017 and references therein). Structural complexity in terms of style and kinematics is commonly associated with strain partitioning at various scales (Fossen et al., 2019). Understanding this evolution requires a variety of methods and techniques. While traditional field-based research has been presented in several recent publications, integrating such results with modern textural analysis (e.g., Cavalcante et al., 2018) is missing in the southern Ribeira belt. Such an approach, which is essential for a better comprehension of the process and

81 mechanisms that lead to strain localization, and consequently, crustal deformation, is
82 required to better understand the nature role of the Lancinha shear zone in the Ribeira
83 belt.

84 In this work, digital geological mapping using the FieldMove Clino and GisKit
85 applications is integrated with detailed micro-scale characterization by means of optical
86 microscopy and SEM-EBSD of selected samples along the LSZ in the South of Brazil.
87 The aim is to investigate the relation between micro- and large-scale structures,
88 kinematic structures, the deformation mechanisms controlling strain localization, and
89 the relationship between grain-size reduction (dynamic recrystallization) and texture
90 development in the orogenic-scale shear zone system of the Ribeira belt.

91

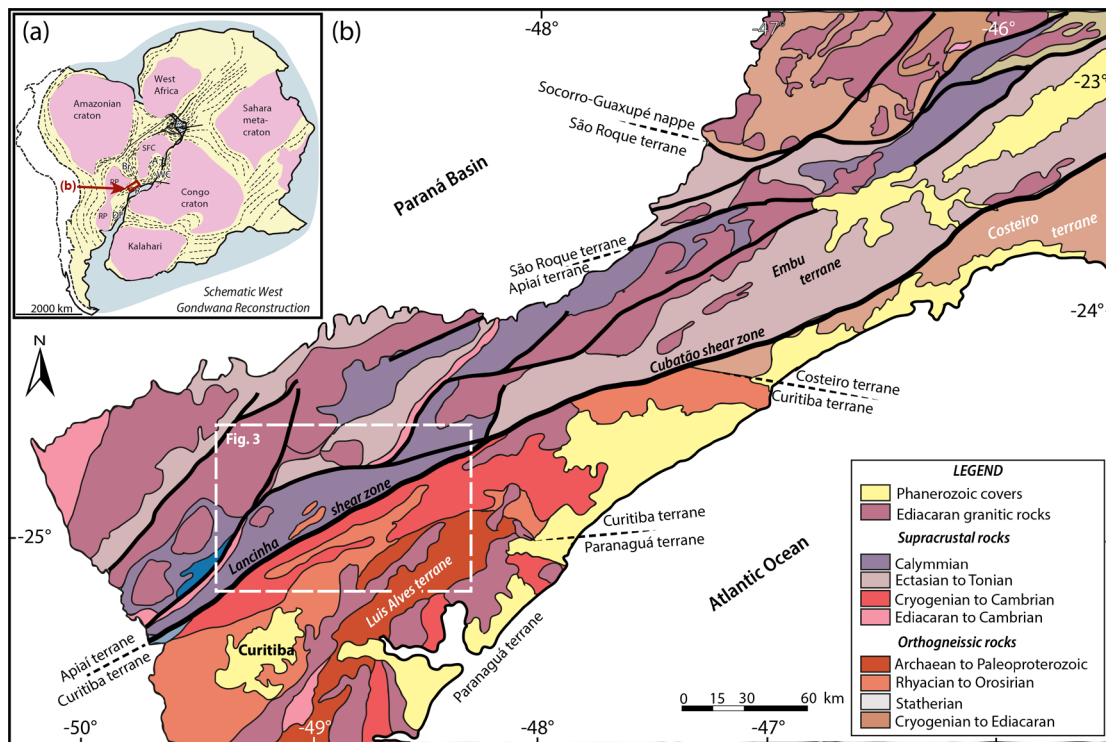
92 **2. GEOLOGICAL SETTING AND SAMPLE DESCRIPTION**

93

94 The southern Ribeira belt (Fig. 1) resulted from the convergence between the São
95 Francisco, Congo and Paranapanema cratons during the amalgamation of west
96 Gondwana, at ~600 Ma (Trompette, 2000). It is characterized by the occurrence of
97 several mostly dextral NE-SW trending strike-slip shear zones in what is considered an
98 overall transpressional orogenic setting (Ebert and Hasui, 1998). The LSZ, together
99 with the Morro do Agudo, Ribeira, Putunã, Serra do Azeite among others shear zones,
100 form part of the anastomosing interconnected shear zone system that characterizes the
101 southern Ribeira belt (Fig. 2). The LSZ is a 150 km long NE-trending strike-slip shear
102 zone, with kinematics often referred to as dextral (e.g. Passarelli et al., 2011; Faleiros et
103 al., 2011, 2016), that separates the Apiaí and Curitiba terranes (Fig. 3) (e.g. James &
104 Assumpção, 1996; Campanha, 2002).

105 Intriguingly, rocks along the Serra do Azeite and Putunã shear zones, that are
106 oriented parallel to the LSZ (Fig. 2), exhibit kinematic indicators such as S-C foliation,
107 σ -porphyroclasts, sigmoidal boudins (e.g. Dehler et al., 2000, 2007), and garnet
108 porphyroblasts with σ -type strain shadows (e.g. Faleiros et al., 2011), all suggestive of
109 sinistral ductile deformation. The Serra do Azeite is interpreted as a transtensional
110 mylonitic shear zone (e.g. Dehler et al., 2000; Machado et al., 2007). K-Ar dating in
111 hornblende and biotite from orthogneisses and in phlogopite from metasediments,
112 provided ages respectively at 565 ± 39 Ma, 527 ± 26 Ma and 587 ± 21 Ma, interpreted
113 as minimum ages for the mylonitic deformation in the Serra do Azeite shear zone

114



115

116 **Figure 1 – (a)** West Gondwana reconstruction with the main cratons (SFC-São Francisco craton; PP-
 117 Paranapanema; RP-Rio de la Plata) and orogenic belts (A-Araçuaí; R-Ribeira; WC-West Congo; DF-
 118 Dom Feliciano). **(b)** Geological map of the Ribeira belt showing the anastomosing shear zone network
 119 and the location of the study area (dashed box). Adapted from Campanha et al., (2015).

120

121

122

123

124

125

126

127

128

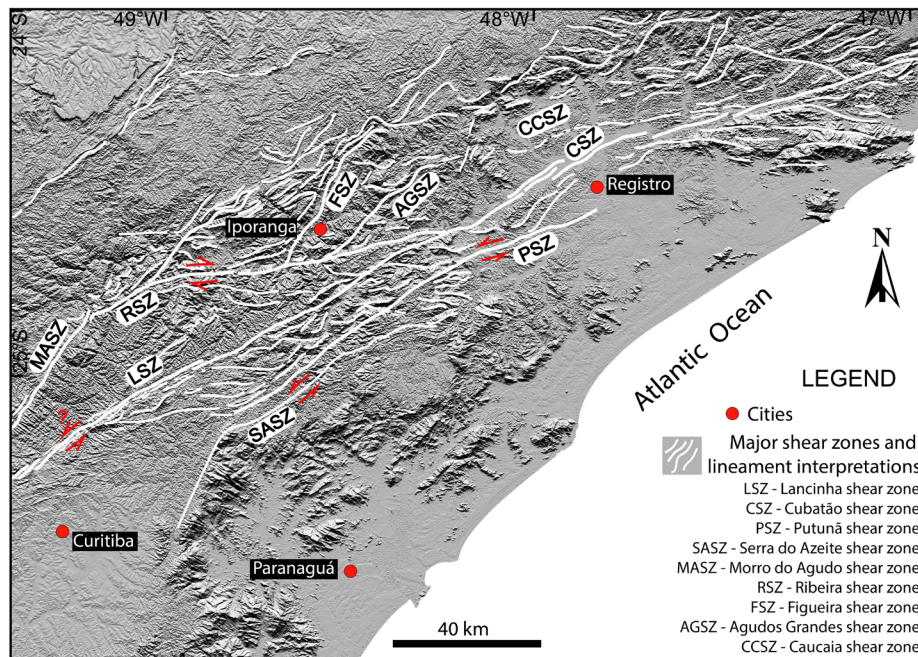
129

130

131

132

133



134 **Figure 2 -** Digital elevation model with lineament interpretations and major shear zones, displaying the
 135 interconnected pattern of shear zones in southern Ribeira belt. Available on
 136 <http://www.webmapit.com.br/inpe/topodata/>.

137

138 (Campagnoli, 1996). Furthermore, a muscovite K-Ar age of 577 ± 3 Ma was interpreted
 139 as the lower limit for the transtensional mylonitic deformation along the Serra do Azeite
 140 shear zone (Machado et al., 2007). Close to the study area, the Putunã shear zone is
 141 interpreted as a greenschist facies sinistral transcurrent shear zone (Faleiros et al.,
 142 2011). A chemical age of 579 ± 8 Ma obtained in monazite from a paragneiss was
 143 interpreted as a minimum age for the low temperature (greenschist facies) fabric
 144 developed along the Putunã shear zone (Faleiros et al., 2011).

145

146

147

148

149

150

151

152

153

154

155

156

157

158

159

160

161

162

163

164

165

166

167

168

169

170

171

172

173

174

175

176

177

178

179

180

181

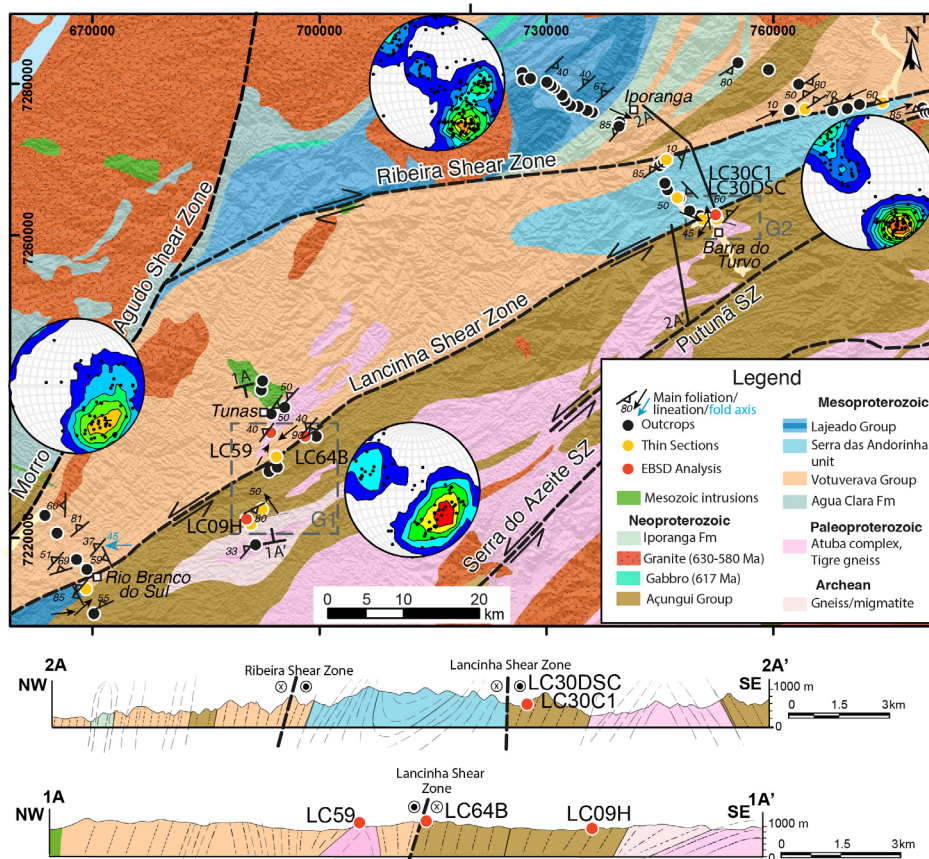
182

183

184

185

186



176 **Figure 3** - Detailed geological map on a digital elevation model of the study area, showing location of
 177 visited localities, samples selected for EBSD analysis, stereoplots for planar fabrics (foliation/cleavage),
 178 and schematic cross sections. Dashed boxes represent groups 1 and 2 (G1 and G2) samples, selected for
 179 EBSD analysis. Based on digital map by the Brazilian Geological Survey (<http://geobank.cprm.gov.br/>),
 180 Faleiros et al., (2012) and Faleiros and Pavan (2013).

181

182

183

184

185

186

187

188

189

190

191

192

193

194

195

The study area consists of the Apiaí and Curitiba terranes (Fig. 1). These terranes include low grade Neoproterozoic and Mesozoic metasedimentary rocks, and Paleoproterozoic to Archean gneissic and migmatitic units (Fig. 3). Deep weathering and limited amounts of outcrops make it difficult to define the LSZ in the study area,

187 but most of the strain appears to be localized in a ≥ 200 m wide zone of sheared rocks.
188 Generally, the rocks show a steep NE-SW to E-W trending foliation, monoclinical folds,
189 slickenlines, S-C structures and a subhorizontal mineral stretching lineation.

190 Sampling was performed along four profiles with 66 outcrops across the Lancinha
191 and Ribeira shear zones (Fig. 3). Six samples representative of the deformation related
192 to the LSZ (Figs. 4, 5) were selected for EBSD analysis and separated into two groups
193 based on microstructural similarities and spatial distribution. One sample from the
194 southernmost part of the LSZ, close to the Rio Branco town, which consists of phyllites
195 with crenulation cleavage (Fig. 4a), did not provide reliable textural analysis data due to
196 technical problems, and was therefore excluded from the CPO section (section 4.2).

197 Group 1 (G1), located in the southern portion of the LSZ, consists of quartzites
198 (samples LC09H and LC59) with thin phyllosilicate-rich layers and mineral lineation
199 characterized by elongated quartz grains (Figs. 4b, 4c), and of mylonitic granite (sample
200 LC64B; Figs. 4e, f). Group 2 (G2), located in the northern portion of the LSZ (Fig. 3),
201 consists of (garnet) schists (samples LC30C1 and LC30DSC) with mineral lineation
202 characterized by shape preferred orientation of quartz grains, and with quartz ribbons
203 with aspect ratio of about 1:5, associated with numerous deformed quartz veins (Fig. 5).
204 They display S-C fabric indicating normal-sinistral sense of shear. These rocks belong
205 to the Açungui Group and Atuba complex (Fig. 3).

206

207 3. ANALYTICAL METHODS

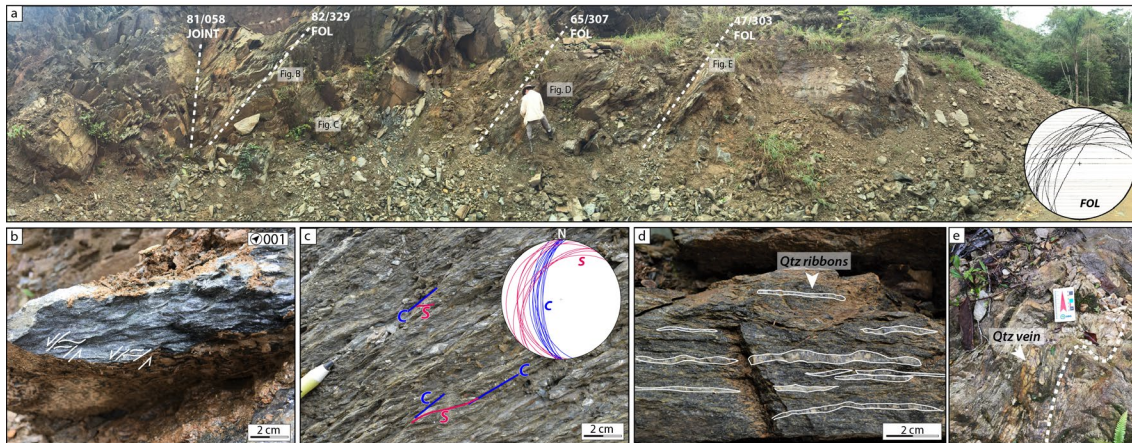
208

209 The thin sections were cut perpendicular to the foliation and parallel to the
210 stretching lineation (XZ plane of the finite strain ellipsoid), followed by 3, 1 and 0.25
211 μm diamond paste polishing and colloidal silica in suspension polishing to remove
212 surface damage. EBSD analysis was conducted with a FEG Quanta 450 and with a
213 Tescan Mira3 LM field emission gun scanning electron microscopes, at the Electron
214 Microscopy Centre (CEM) and at the Materials and Structures Laboratory (LAME) at
215 the Lactec Institute, at the Paraná Federal University (UFPR), Brazil. Operating
216 conditions were at 20 kV accelerating voltage, 15 mm of working distance, 70°
217 specimen tilt, and a step-size ranging from 1.2 to 3.40 μm . An Oxford Nordlys Nano
218 EBSD detector was used for measuring diffraction patterns, which were collected and
219 indexed using the AZtec software from Oxford Instruments. An OIM AnalysisTM

220 software from EDAX instruments was also used for acquisition and treatment of EBSD
 221 patterns.
 222



223
 224 **Figure 4** – Pictures of outcrops representative of the Group 1 rocks: (a) Phyllites with crenulation
 225 cleavage; (b) elongated quartz grains characterizing the stretching lineation in quartzite; (c) quartzite with
 226 steeply dipping foliation; (d) The continuous foliation of the phyllitic rocks; (e) mylonitic granite with
 227 sub-vertical foliation and; (f) detail of the mylonitic foliation in Fig. 4e.
 228
 229
 230
 231
 232



233
 234 **Figure 5** – (a) Picture of schist outcrop representative of Group 2 rocks. White dashed lines indicate the
 235 foliation and joint traces, and the stereoplot shows the orientation of the foliation; (b) and (c) S-C fabric
 236 indicating normal-sinistral sense of shear. The stereoplot displays the S and C orientations; (d) quartz
 237 ribbons; (e) folded quartz vein.

238

239

240

The acquired EBSD data were processed for texture analyses using the MTEX
 241 toolbox (Hielscher and Schaeber, 2008; Bachmann et al., 2010), version 4.5.0, for
 242 Matlab™, from which pole figures (PF), phase and Euler angle maps, inverse pole
 243 figures (IPF), and misorientation histograms were produced. Grain-size distribution
 244 histograms were produced using the CHANNEL 5 software from Oxford Instruments.
 245 To establish reliable correlations and comparisons, EBSD data from all samples have
 246 undergone a unique cleaning routine, where EBSD pixels with the mean angular
 247 deviation (MAD) higher than 1.2° and grains with less than 2 indexed points were
 248 excluded. Grain boundaries were defined at misorientation angle $>10^\circ$. The grain-size
 249 distribution was calculated from EBSD orientation maps based on 2D area fraction,
 250 using weighted grain areas, with each grain having at least 100 pixels and samples
 251 having more than 500 grains (e.g. Herwegh 2000; Berger et al., 2011; ASTM E2627-13,
 252 2019). For each sample, [c], <a> directions, and poles for crystallographic planes {m},
 253 {r}, and {z} in quartz were plotted.

254

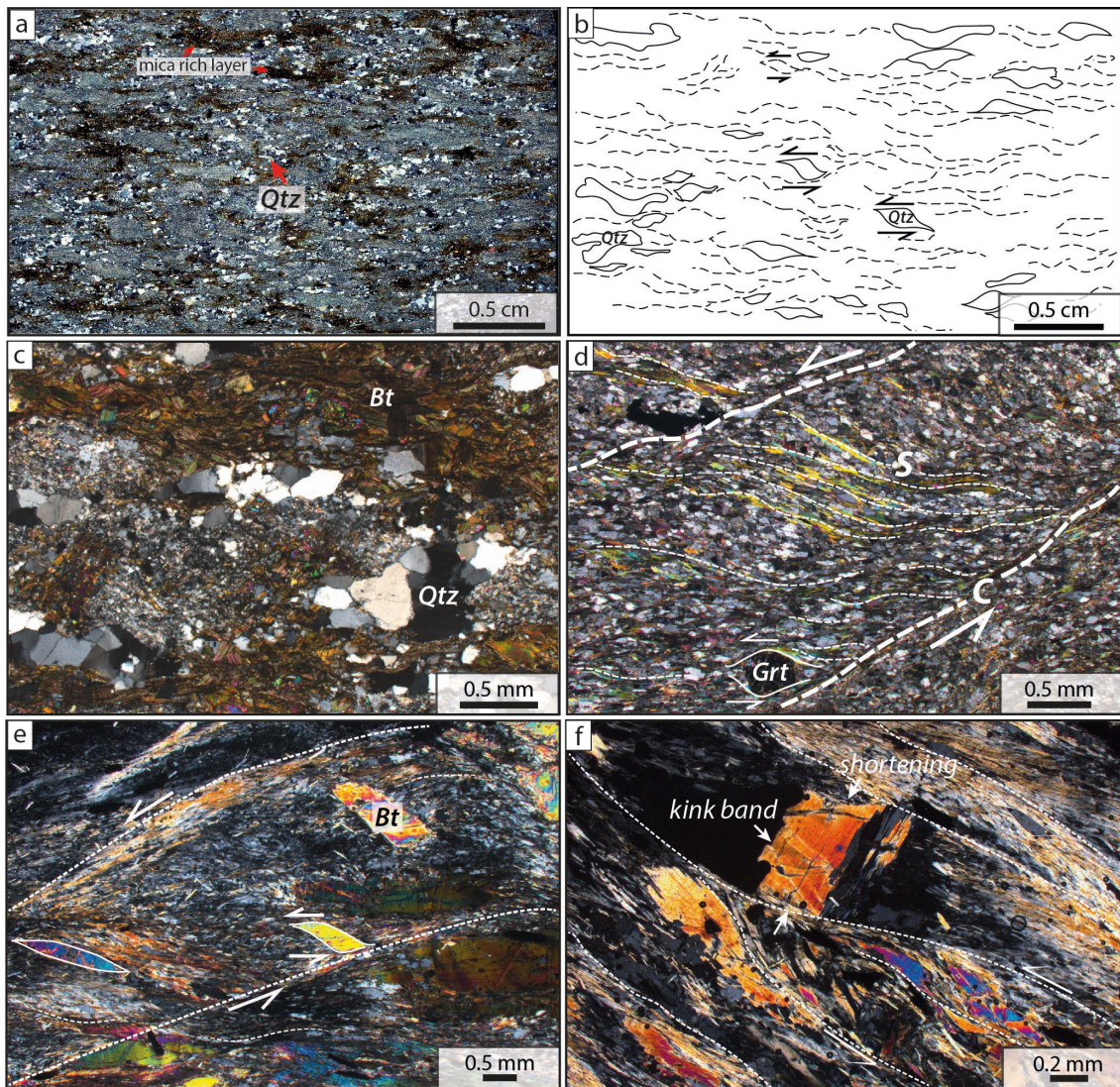
255 4. RESULTS

256

257 4.1. Fabric elements and microstructures

258

259 The most striking textural feature observed from a total of seventeen thin
 260 sections from the LSZ and adjacent areas (Fig. 3) is the microscale alternation of quartz-
 261 and mica-rich layers that defines an anastomosing foliation (Fig. 6a). Quartz layers



263
 264 **Figure 6** – Image of scanned thin sections (crossed polarizers) and optical photomicrographs of
 265 microstructures from representative rocks exposed along the Lancinha and correlated shear zones. **(a)**
 266 Alternating recrystallized quartz aggregates and muscovite-rich layers characterize the anastomosing
 267 foliation. Asymmetric shapes of quartz aggregates indicate sinistral sense of shear, highlighted in the
 268 sketch **(b)**; **(c)** Strain-free and weakly deformed quartz grain agglomerates exhibiting straight and
 269 irregular boundaries, within fine-grained quartz-mica matrix; **(d)** S-C type of anastomosing foliation and
 270 rotated garnet porphyroblast indicating sinistral sense of shear in schists; **(e)** Biotite with fish geometry
 271 indicating sinistral sense of shear; **(f)** Biotite with kink bands as observed in schist.

272

273 consist of recrystallized asymmetric aggregates indicating sinistral sense of shear (Fig.
 274 6b). Metasedimentary rocks from the Açungui Group also exhibit agglomerates of
 275 coarse quartz grains (0.3 mm diameter), often optically strain-free, or with weak
 276 undulose extinction and straight and irregular boundaries, among randomly oriented
 277 biotite grains, which reach up to 1 mm in size (Fig. 6c).

278 Quartz recrystallized grains from quartzites range in size from 10 to 50 μm .
 279 Schists have coarse-grained (50 to 200 μm) quartz, which occurs as recrystallized bands

280 that, along with thin mica layers, commonly form a S-C fabric, which suggests sinistral
281 sense of shear (Fig. 6d). Mica grains with fish geometry and garnet porphyroblasts also
282 indicate sinistral sense of shear (Figs. 6d, e, f). Undulose extinction and deformation
283 bands in mica often occur both in quartzites and schists. The schists also show mica
284 kink bands (Fig. 6f).

285

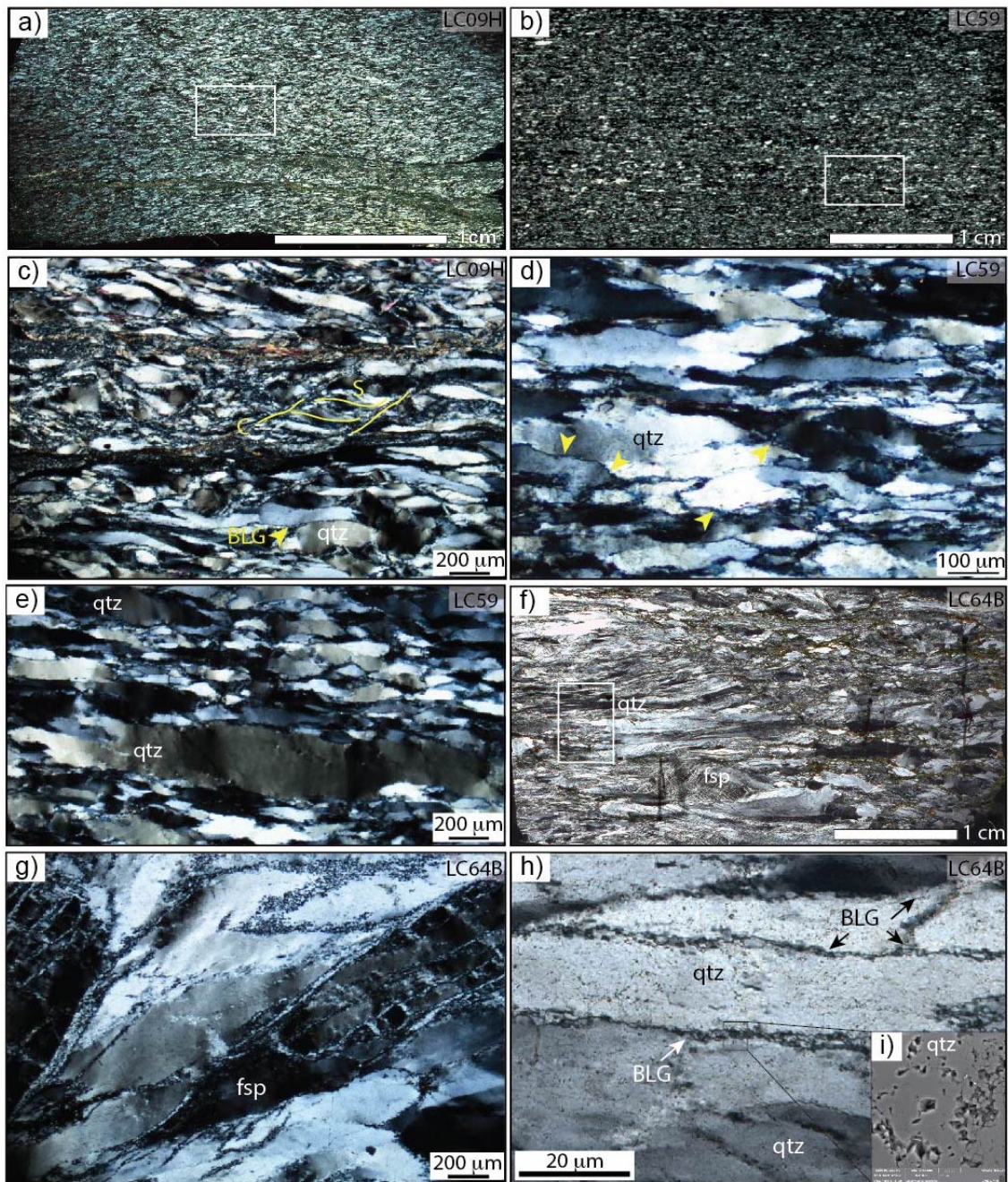
286 *4.1.1. Group 1 (G1) microstructures*

287

288 This group (Fig. 3) is represented by quartzites (samples LC09H and LC59;
289 Figs. 7a, b) and by granitoid with mylonitic foliation (sample LC64B). Quartzites are
290 composed of inequigranular quartz aggregates and quartz ribbons (95%) and thin mica
291 layers. Quartz grains with strongly flattened shapes have sizes ranging from 50 to 400
292 μm long (Fig. 7c). They often form wavy ribbons with an aspect ratio of 1:3 and sigma
293 shapes, that together with thin layers of phyllosilicates, characterize the anastomosing
294 foliation, locally arranged in a S-C geometry in which S consists of wavy elongated
295 quartz and C of recrystallized quartz grains (Fig. 7c). Quartz often shows strong shape
296 preferred orientation and serrated grain boundaries suggestive of bulging (BLG)
297 recrystallization (Figs. 7c, d), few subgrains and few new grains with sizes close to the
298 subgrain sizes, undulose extinction and deformation bands (Fig. 7e).

299 The mylonitic granitoid (sample LC64B) consists of quartz (50%), feldspar (40%)
300 and phyllosilicates (10%). The mylonitic foliation is characterized by elongated quartz
301 ribbons surrounding feldspar porphyroclasts (Fig. 7f). The feldspar porphyroclasts are
302 strongly fractured. Very small grains consisting mostly of feldspar occur along their
303 fractures and margins (Fig. 7g), and such small feldspar grains, as compared to the
304 parent grains, suggest recrystallization by BLG or result of classical nucleation (e.g. Fitz
305 Gerald and Stünitz, 1993). Quartz grains with undulose extinctions and few subgrains
306 sometimes display sigmoidal shape ($\sim 50 \mu\text{m}$ long); quartz ribbons have aspect ratio of
307 $\sim 1:4$ and are often surrounded by small recrystallized grains (up to $10 \mu\text{m}$ in size), with
308 serrated grain boundaries (Figs. 7h, i) typical of BLG recrystallization (e.g. Stipp et al.
309 2002b).

310



311
 312 **Figure 7** - Microstructures from rocks of the G1. **(a)** and **(b)** Scanned images of thin section with
 313 polarized light displaying the general aspects of quartzites; **(c)** Flattened quartz grains exhibiting
 314 sweeping undulatory extinction, arranged along an anastomosing foliation that locally forms a S-C
 315 geometry, and small quartz grains probably formed by BLG recrystallization, along grain boundaries
 316 (yellow arrow); **(d)** Elongated quartz grains exhibiting undulose extinction and serrated grain boundaries
 317 (yellow arrows) suggestive of BLG recrystallization; **(e)** quartz ribbons with undulose extinction,
 318 subgrains, and irregular serrated grain boundaries; **(f)** Image of scanned thin section (crossed polarizers)
 319 from sample LC64B displaying the general aspect of the mylonitic granite; **(g)** Fractured feldspar
 320 porphyroclast in the mylonitic granite, with very small grains occupying its fractures and margins; **(h)**
 321 Detailed photomicrography from sample LC64B showing recrystallized BLG domains at quartz serrated
 322 grain boundaries and; **(i)** BSE image displaying the very small (<10 μm) serrated quartz grain boundaries.
 323 White boxes in the scanned images are areas selected for EBSD analysis.

324

325

326 4.1.2. Group 2 (G2) microstructures
327

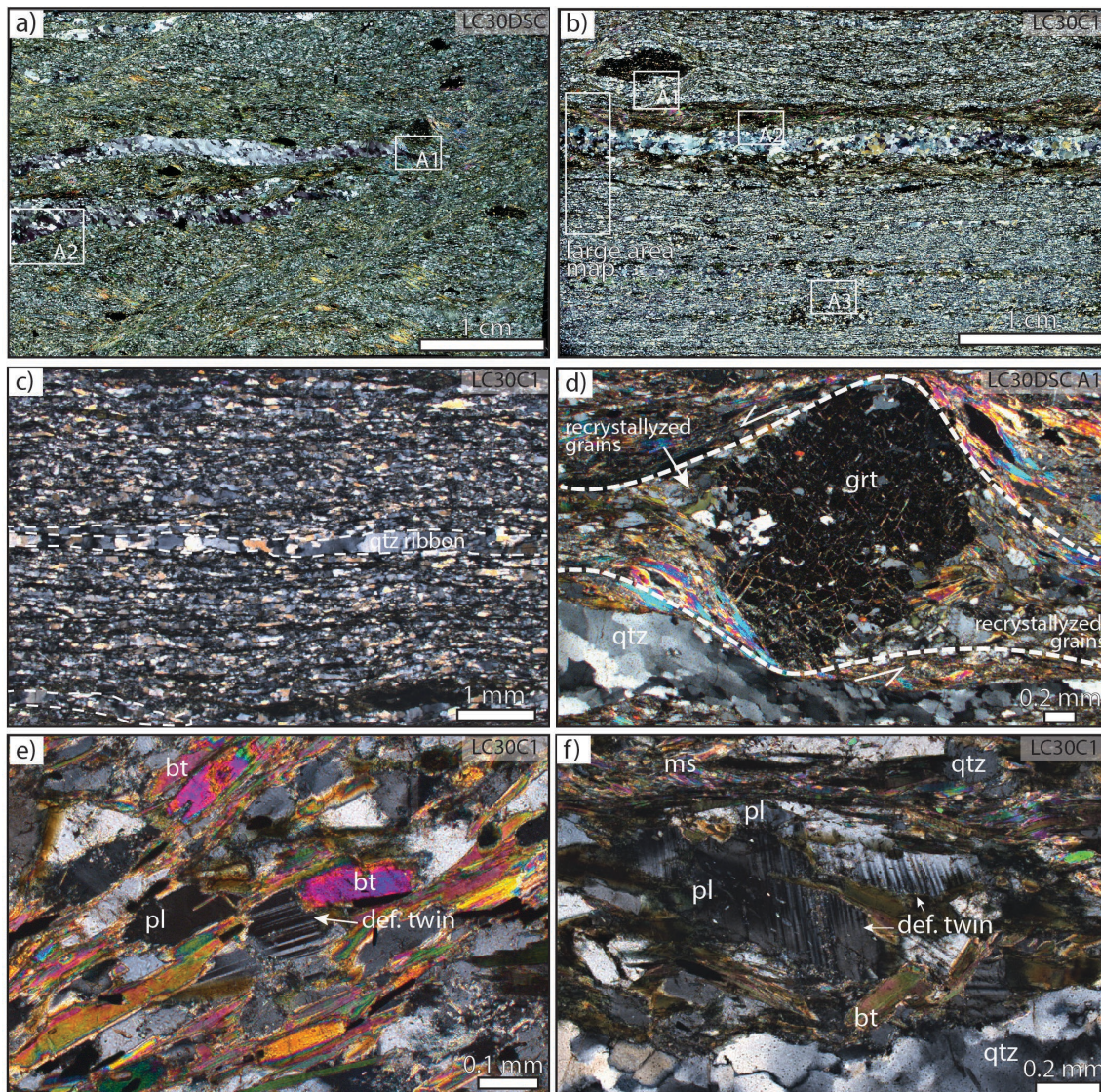
328 Samples from this group (LC30DSC and LC30C1) consist of (garnet) quartz-
329 schist that contains strongly shape-oriented phyllosilicates (mainly biotite), K-feldspar,
330 plagioclase, amphiboles and epidote. Quartz is abundant (70%) and occurs as: (i)
331 recrystallized bands in which grain size ranges from 50 to 200 μm ; (ii) strongly
332 recrystallized grains in the matrix (Figs. 8a, b), with grain size ranging from >10 to 50
333 μm and boundaries mainly irregular serrated, suggestive of BLG recrystallization and;
334 (iii) layers with subgrains/new grains oriented oblique to the foliation, suggestive of
335 SGR recrystallization. Quartz also occurs as polycrystalline ribbons with aspect ratios
336 of 1:7, commonly with lobate grain boundaries suggestive of grain boundary migration
337 (GBM) recrystallization (Fig. 8c). Garnet porphyroblasts, reaching up to 5 mm in
338 diameter, show quartz inclusions and recrystallized quartz in pressure shadows,
339 indicating sinistral sense of shear (Fig. 8d). Biotite grains distributed in the matrix often
340 characterize a S-C geometry and show undulose extinction and kink bands. Plagioclase
341 grains show undulose extinction and deformation twinning and are surrounded by
342 biotite with strong preferred orientation (Figs. 8e and f). Undulose extinction also
343 occurs in amphibole grains that have sigmoidal shapes.

344

345 4.2. Crystallographic preferred orientation (CPO) - Textural analysis
346

347 Quartz crystallographic orientations were measured in all samples from the two
348 groups (G1 and G2). The selected EBSD areas are shown in Figures 7a, b, f and Figures
349 8a, b, and the pole figures (PF) and inverse pole figures (IPF) are presented in Figure 9
350 and Figure 10. The EBSD maps are available in the supplementary material. All PFs
351 calculated from ODF (orientation distribution function) are shown with the foliation
352 oriented E-W and vertical, and the lineation oriented E-W and horizontal, represent one
353 point per grain measurement, and they all represent X-Z sections of the finite strain
354 ellipsoid. Inference of active slip systems were based on the assumption that CPO
355 skeletons or maxima result from the activity of dominant slip systems (e.g. Lister et al.,
356 1978; Price, 1985).

357



358
 359 **Figure 8** – Microstructures from rocks of the G2. **(a)** and **(b)** Image of scanned thin section with
 360 polarized light from quartz-schists showing the distribution of quartz grains in recrystallized bands and in
 361 the matrix (highlighted white boxes represent the selected areas for EBSD analysis); **(c)** Polycrystalline
 362 quartz ribbon exhibiting lobate grain boundaries; **(d)** Garnet porphyroblast with recrystallized quartz
 363 grains in pressure shadows indicating sinistral sense of shear, and quartz rich layer with oblique subgrains
 364 (lower part of the image); **(e)** and **(f)** Plagioclase grains with undulose extinction and deformation twins
 365 surrounded by biotite with strong preferred orientation **(e)** and arranged in a S-C fabric (upper right side
 366 in **f**).

367

368

369 4.2.1. Group 1 (G1) quartz crystallographic orientation

370

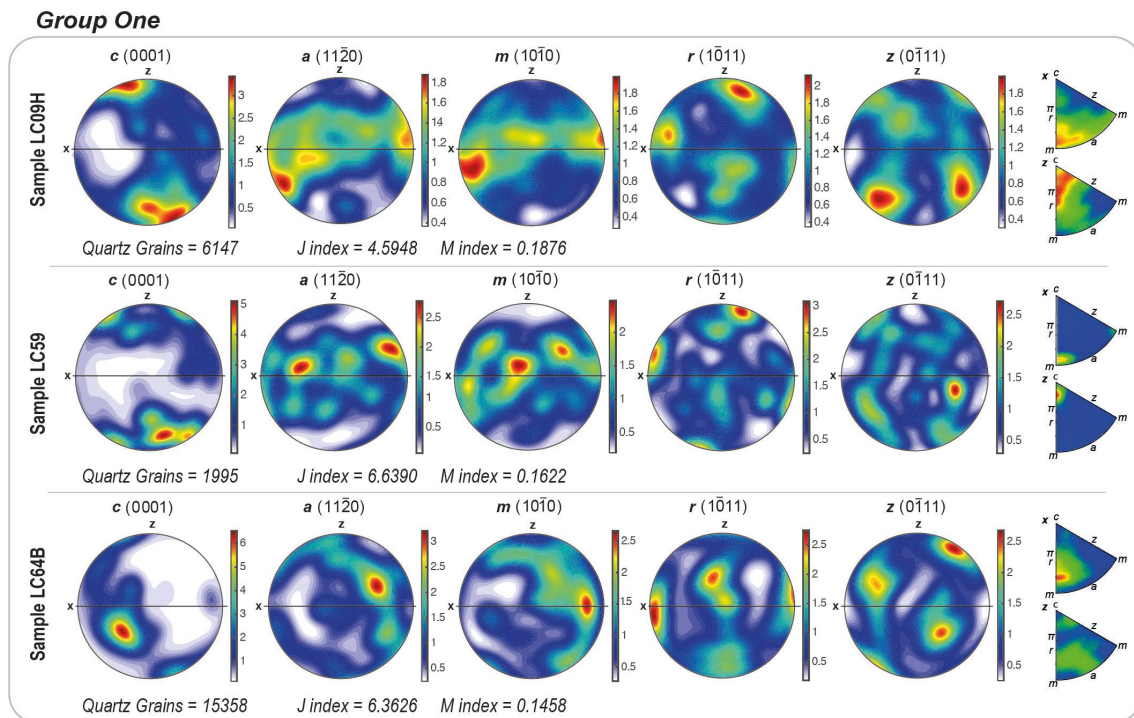
371 PFs from samples LC09H and LC59, both from quartzites, show a strong
 372 concentration of quartz c-axis at 15-30° counterclockwise to the pole of the foliation (Z)
 373 and <a> axis with a broad distribution along the foliation plane, with weak
 374 concentrations close to X, consistent with basal <a> slip (e.g. Little et al., 2013) and

375 sinistral sense of shear (Fig. 9). Poles to $\{m\}$ planes are distributed along great circles
376 with weak maxima close to X (LC09H) and Y (LC59) (Fig. 9). Rhomb planes $\{r\}$ and
377 $\{z\}$ show a wide distribution with maxima with different strengths close to Z and X, and
378 at high angle to X. Maxima close to Z point to some slip along rhomb $\{r\}$ planes, a slip
379 system also inferred from the IPF for sample LC09H (e.g. Schmid and Casey, 1986).
380 Activation of both basal $\langle a \rangle$ and rhomb $\langle a \rangle$ together with evidence of dominant BLG
381 recrystallization suggest quartz from quartzites deformed under low temperature
382 conditions ≤ 400 °C (e.g. Stipp et al., 2002b).

383 Sample LC64B displays $\langle c \rangle$ axis distributed along a broad great circle that runs
384 from northwest to southeast, with a small-circle maximum oblique to X (Fig. 9). $\langle a \rangle$
385 axis and poles to $\{m\}$ show a similar texture that defines a broad great circle running
386 from northwest to southeast, with a weak cluster at $\leq 30^\circ$ ($\langle a \rangle$ axis) and close to X ($\{m\}$
387 poles). $\{r\}$ and $\{z\}$ planes are quite dispersed, with small concentrations close to X and
388 at $\sim 30^\circ$ clockwise to Z. Although $\{z\}$ planes are oriented favorable for slip, activation
389 of rhomb $\langle a \rangle$ is unlikely due to the $\langle a \rangle$ axis orientation being oblique to X.

390 G1 IPFs for X and Z directions show a gentle concentration of $\{m\}$ and $\langle a \rangle$ close
391 to the X direction, while $\langle c \rangle$ axis clearly concentrates close to Z, especially for the
392 quartzites samples (LC09H and LC59), as well as some positive rhomb planes. Such a
393 distribution reiterates the suggestion of the activation of basal $\langle a \rangle$ slip, with some
394 contribution of rhomb $\langle a \rangle$ slip, especially for sample LC09H. For the mylonitic granite
395 (LC64B), IPF and pole figures do not allow for a conclusive interpretation in terms of
396 slip systems.

397



398

399 **Figure 9** - Quartz crystallographic orientations for rocks from G1. Pole and Inverse pole figures (IPF).
 400 Pole figures are represented at lower hemisphere equal-area projections. IPFs are represented for X (upper
 401 right corner) and Z directions (lower right corner). The densities of poles diagrams were color-coded and
 402 contoured in Multiples of a Uniform Distribution (M.U.D.), defined by the scale bar on the right of each
 403 pole figure.

404

405 4.2.2. Group 2 (G2) quartz crystallographic orientation

406

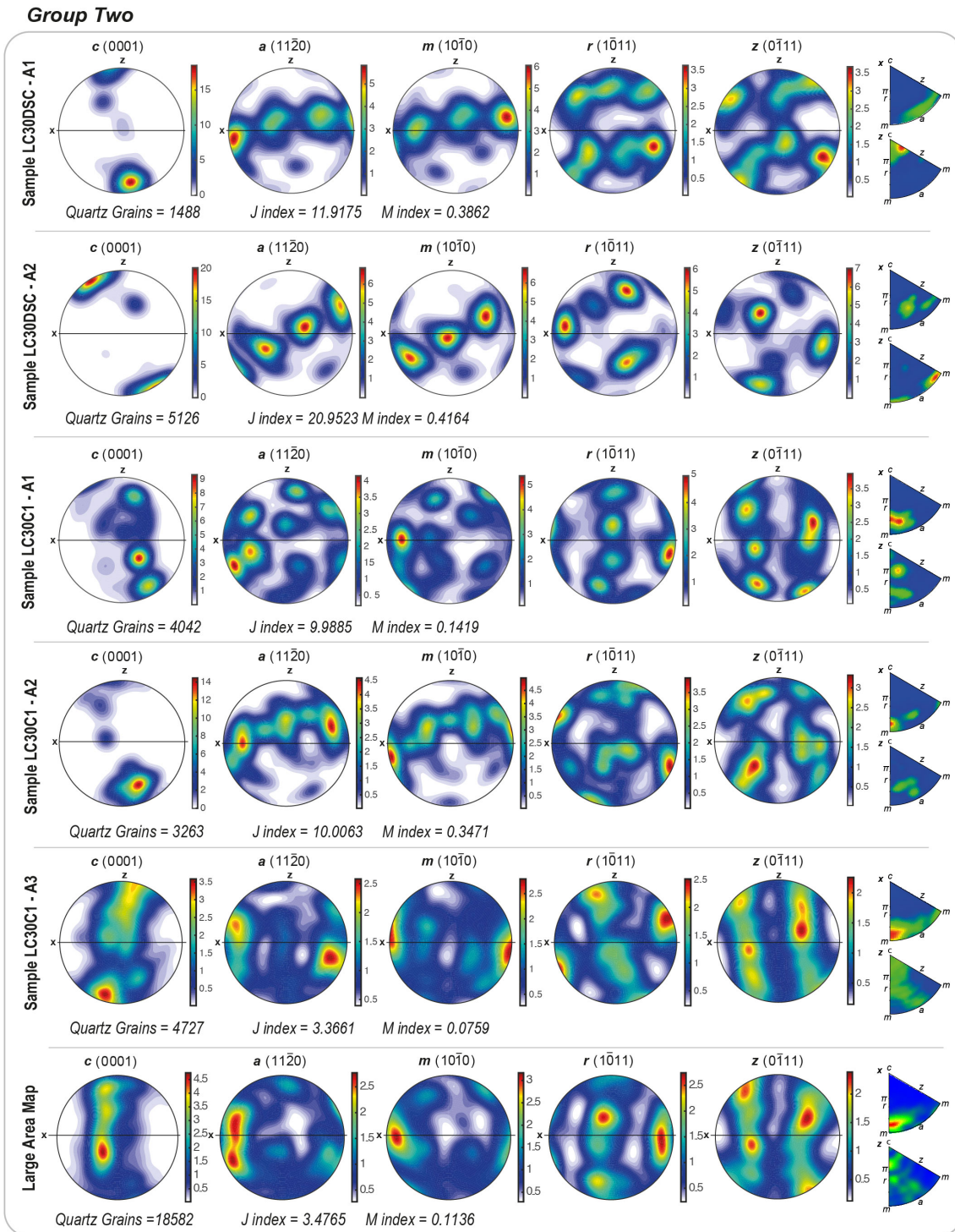
407 The two areas (A1 and A2) selected for EBSD analysis (Fig. 8a) on sample
 408 LC30DSC display similar textures (Fig. 10). $\langle c \rangle$ axes display well-defined small circles
 409 located at the periphery oblique to the foliation, at $\sim 30^\circ$ counterclockwise to Z,
 410 consistent with sinistral sense of shear and basal $\langle a \rangle$ slip (e.g. Schmid and Casey, 1986;
 411 Mancktelow and Pennacchioni, 2004). $\langle a \rangle$ and poles to $\{m\}$ are distributed along
 412 girdles normal to $\langle c \rangle$, with strong concentrations close to X. Poles to rhomb $\{r\}$ define
 413 a cleft girdle distribution according to Lister and Hobbs' (1980) classification. Poles to
 414 rhomb $\{z\}$ define a crossed girdle for area A1 and three scattered maxima for area A2.
 415 IPF figures for this sample are concentrated around $\{m\}$ and $\langle a \rangle$ for the X direction,
 416 and around $\langle c \rangle$ and $\{m\}$ for the Z direction for areas A1 and A2, respectively. Such an
 417 IPF distribution, even if it is not clear, is still consistent with activation of basal $\langle a \rangle$
 418 slip, and also with some prism $\{m\}$ planes oriented favorable for slip.

419 Four areas were selected on sample LC30C1 (A1, A2, A3 and Large Area Map;
420 Fig. 8b). Quartz from Area A1 display $\langle c \rangle$ axes distributed along a single narrow girdle
421 that runs from northwest to southeast, at a small angle counterclockwise to Z,
422 suggestive of sinistral sense of shear and some activity of basal $\langle a \rangle$ slip (Fig. 10). Poles
423 to $\{m\}$ and $\langle a \rangle$ exhibit similar texture with several maxima that define a few main
424 concentrations close to X and at $\sim 30^\circ$ to X, respectively. Poles to rhomb $\{r\}$
425 characterize a single narrow girdle that runs from north to south and a small circle close
426 to X. Poles to rhomb $\{z\}$ define a north-south cleft girdle (e.g. Little et al., 2013). IPFs
427 display some grains with $\langle a \rangle$ axis oriented parallel to X and positive rhomb planes
428 favorably oriented for slip, suggestive of rhomb $\langle a \rangle$ activity.

429 Quartz from Area A2 show $\langle c \rangle$ axis distribution forming several small oblique
430 maxima that extend toward the center, almost defining a single girdle, with main
431 maximum at $\sim 20^\circ$ counterclockwise to Z, suggesting sinistral sense of shear, basal $\langle a \rangle$
432 slip, and some rhomb slip (e.g. Heilbronner and Tullis 2006; Fig. 10). Additional
433 activation of rhomb $\langle a \rangle$ slip can also be suggested from the IPF map, which includes
434 certain grains with rhomb $\{r\}$ planes favorably oriented for slip and some grains with
435 $\langle a \rangle$ axes close to X. $\langle a \rangle$ axes and poles to $\{m\}$ are distributed along great circles
436 normal to $\langle c \rangle$ axis main maximum. Poles to $\{r\}$ are spread out, but weak maxima at
437 $\sim 20^\circ$ to the lineation and close to Z can be observed. Poles to $\{z\}$ define a diffuse cleft
438 girdle, which runs from north to south.

439 Quartz from Area 3 displays $\langle c \rangle$ axis distributed along a broad girdle that runs
440 from northeast to southwest at a small angle clockwise to Z, indicative of dextral sense
441 of shear (Fig. 10). There are also indications of basal $\langle a \rangle$ and rhomb $\langle a \rangle$ slip, also
442 noticeable from the IPF diagram, with $\langle a \rangle$ axes oriented parallel to X and rhomb and
443 basal planes oriented favorable for slip. $\langle a \rangle$ and poles to $\{m\}$ have similar texture with
444 a wide distribution, although small maxima on the perimeter on either side of X occur.
445 Poles to $\{r\}$ present a wide distribution with three weak concentrations close to X and
446 Z. Poles to $\{z\}$ define a broad cleft girdle.

447 $\langle c \rangle$ axes are distributed along a single broad symmetric girdle that runs from
448 north to south, with a strong concentration close to Y, pointing to an important activity
449 of prism $\langle a \rangle$ slip (e.g. Schmid and Casey, 1986; Stipp et al., 2002a; Mancktelow and
450 Pennacchioni, 2004) and a strong component of coaxial deformation. Poles to $\{m\}$ and
451 $\langle a \rangle$ axes show a rather scattered distribution with weak concentrations around X.



452

453 **Figure 10** – Quartz crystallographic orientations for rocks from G2. Pole and Inverse pole figures (IPF).
 454 Pole figures are represented at lower hemisphere equal-area projections. IPFs are represented for X (upper
 455 right corner) and Z (lower right corner) directions. The densities of poles diagrams were color-coded and
 456 contoured in Multiples of a Uniform Distribution (M.U.D.), defined by the scale bar on the right of each
 457 pole figure.

458

459 Poles to rhomb planes are also scattered, but some weak concentrations of {r}
 460 poles close to X and around Y and Z occur. Evidence of secondary activity of rhomb

461 <a> slip in the IPFs, which display certain grains with <a> axis oriented parallel to X
462 and rhomb forms favorably oriented for slip, is also observed. Poles to {z} define a sort
463 of broad cleft girdle running from north to south.

464

465 4.2.3. Grain size distribution (GSD)

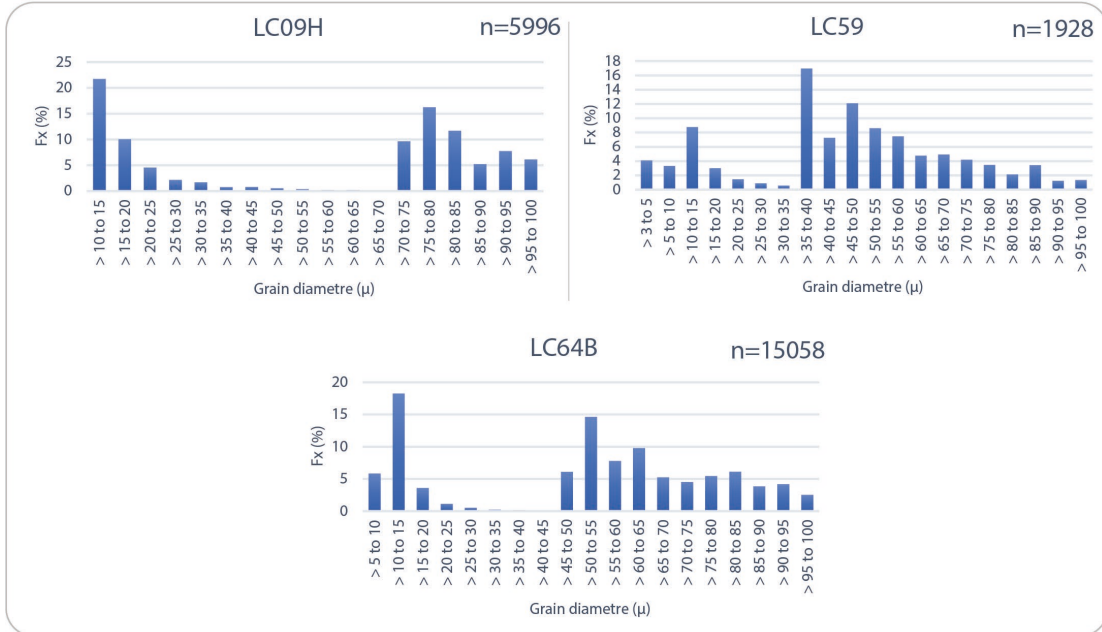
466

467 Grain size distribution for quartz from all samples is presented in Figure 11.
468 Quartz in quartzites from G1 have similar grain-size distribution, with ~50% of grains
469 from the EBSD mapped area being up to 50 μm in diameter. These grains represent
470 recrystallized grains. The main concentration of recrystallized grains occurs at >10-15
471 μm (20%) in sample LC09H, and at >35-40 μm (17%) in sample LC59. The percentage
472 of recrystallized grains in the EBSD mapped area of the mylonitic granite (LC64B) is
473 smaller than for the quartzites, consisting of ~35% of grains with up to 50 μm diameter.
474 The main peak occurs at grains with >10-15 μm (18%).

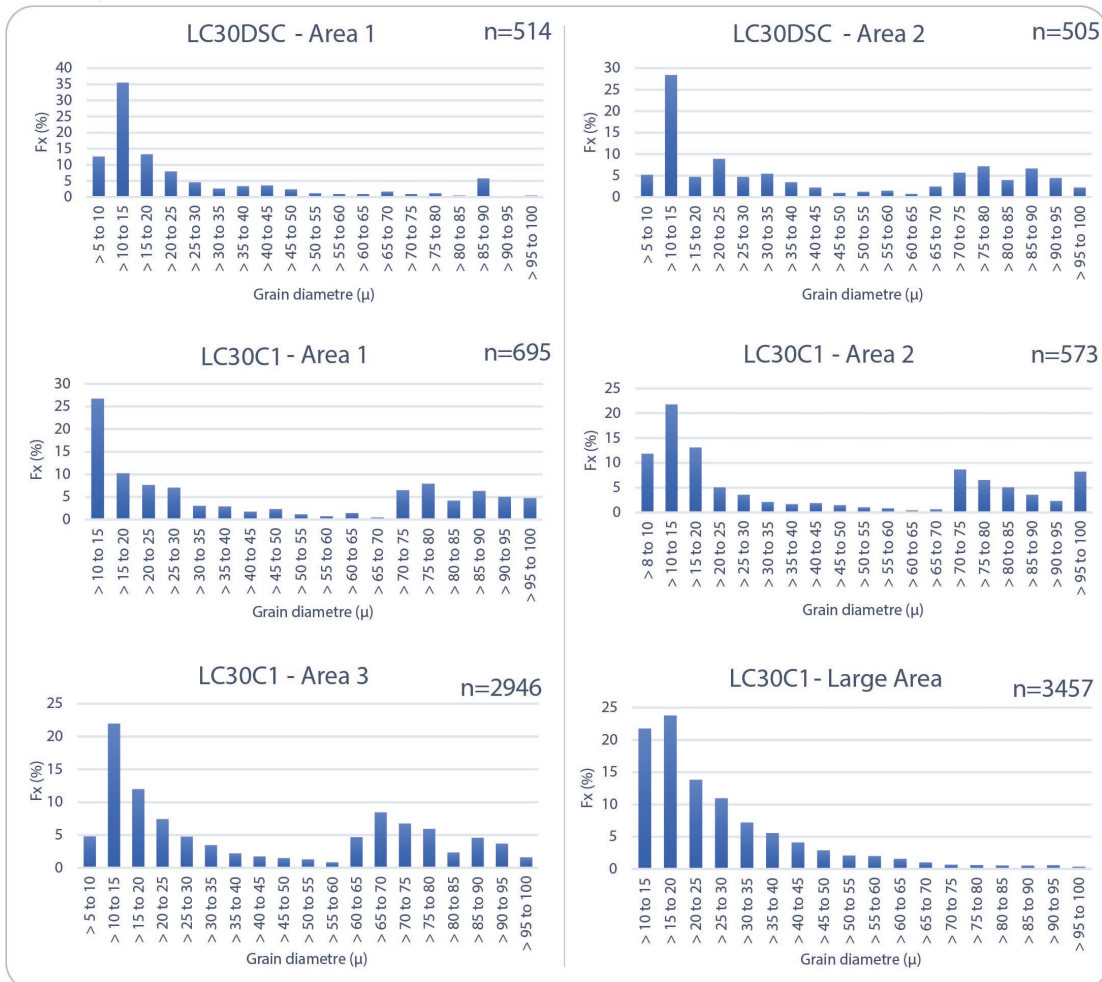
475 Recrystallized quartz grains from the EBSD mapped area in schists from G2 reach
476 200 μm in size. Recrystallized grains with very small sizes (up to 50 μm) make up
477 between 50 to 80% of the EBSD mapped area for both samples (LC30DSC and
478 LC30C1). In the two areas in sample LC30DSC the percentage of recrystallized grains
479 is ~90%. The main peaks of grain sizes occur at >10-15 μm for both areas, being 35%
480 in LC30DSC - Area 1 and ~27% in LC30DSC – Area 2.

481 Recrystallized grains from the four areas in sample LC30C1 represent between 50
482 (Area 2) and 100% (Area 3) of the EBSD mapped area. LC30C1-Area 1, LC30C1-Area
483 2 and LC30C1-Area 3 have main grain size peaks at >10-15 μm (>20-25%). LC30C1-
484 Large area map has two main grain-size peaks at >15-20 μm and at >10-15 μm (>20-
485 25%).

Group One



Group Two



486

487 **Figure 11** – Quartz grain-size frequency diagrams for samples from G1 and G2 (n=number of grains).

488

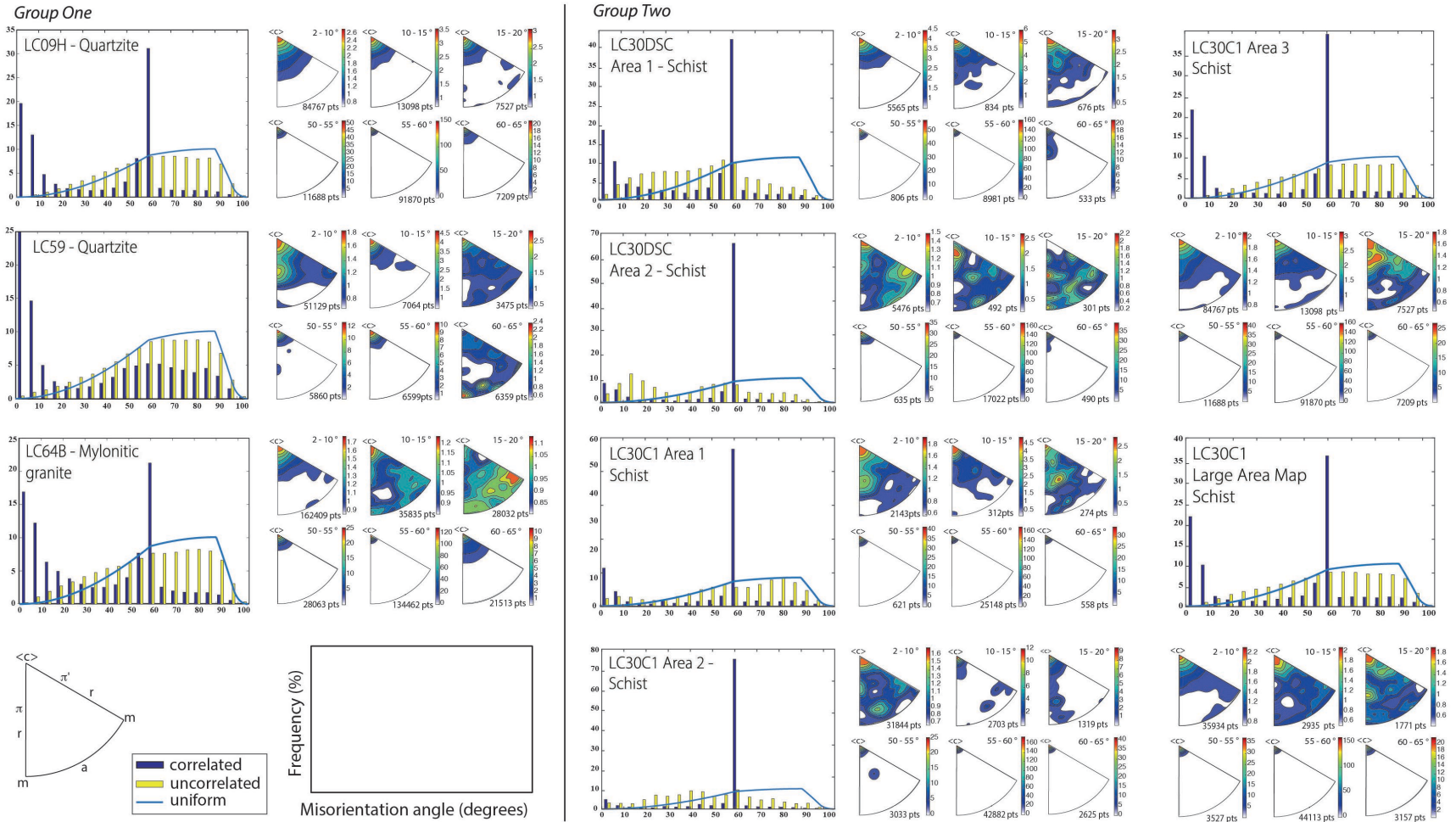
4.2.4. *Misorientation angle distribution*

489
490
491
492
493
494
495
496
497
498
499
500
501
502
503
504
505
506
507
508
509
510
511
512
513
514
515
516
517
518
519
520
521
522
523
524

The misorientation angle distribution for quartz grains are represented in frequency histograms for G1 and G2 samples in Figure 12. The angle of misorientation is the angle between one crystal lattice orientation and its neighbor and can be expressed by a rotation axis and rotation angle (Wheeler et al., 2001). The misorientation histograms were plotted from the mean grain orientation for grain segmentation with a minimum misorientation angle of 2°. Misorientation analysis of grain boundaries were performed for uncorrelated (random pairs) and correlated (neighbor pairs) distribution of angles.

Quartz misorientation angles histograms for all samples from G1 and G2 show one sharp peak at high angles close to 55-60° (except the LC59 from G1), associated with rotation axes in [0001], indicating the presence of Dauphiné Twinning (e.g. Neumann, 2000; Menegon et al., 2010; Wenk et al., 2011). Samples from G1 and LC30C1 (Area 3 and Large Area Map) and LC30DSC (Area 1) from G2 also display a secondary peak at <15°, which suggest the presence of some subgrain boundaries (e.g. Wheeler et al., 2001; Menegon et al., 2010). The rotation axes tend to be aligned parallel to [0001]. The histograms show also some high-angle boundaries in the interval between >15 and 100°, especially for G1 samples. All samples except the LC59 show maxima for the misorientation axes in the 60-65° range parallel to the c-axis, which could be related to activity of the prism slip system {m} < a >. However, in the pole figure plot (Figs. 9, 10), some concentrations of c-axis around the Y-axis is only observed for sample LC30C1 (Area 1, Area 3 and Large Area Map) from G2. Thus, for all the other samples the misorientation axes in the 60-65° range parallel to the c-axis is again interpreted as indicative of Dauphiné twin boundaries. Additionally, most samples show uncorrelated misorientation angles between 20 and 50° with higher frequency than expected for a uniform distribution, whereas misorientation greater than 50° for both correlated and uncorrelated grains occur with a lower frequency than expected for a uniform distribution, in all samples.

525



526
527

Figure 12 - Misorientation angle distribution histograms for quartz from samples from G1 and G2.

528

529 **5. DISCUSSION**

530

531 5.1. Interpretation of (micro) structures and CPO data

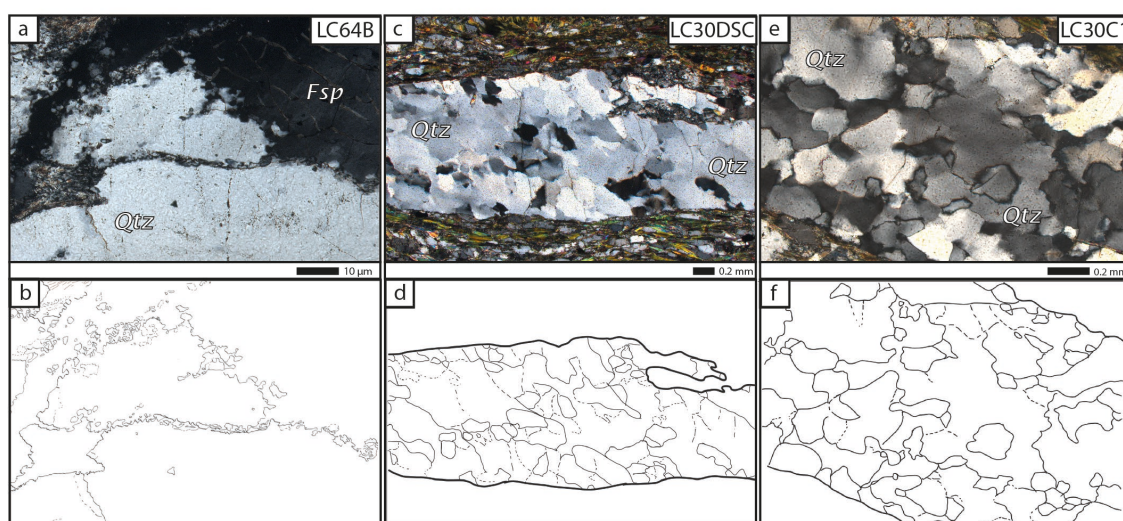
532

533 From field, microstructural observations and textural analysis (EBSD data) on
534 rocks from two groups (G1 and G2) in the Lancinha shear zone and associated shear
535 zones, four main characteristics can be highlighted: (1) intense grain-size reduction with
536 recrystallized grains (up to 50 μm in G1 and up to 200 μm in G2) constituting between
537 50 and 100% of the EBSD mapped areas (Fig. 11) in most samples, except the sample
538 LC64B mylonitic granite, which recrystallized grains make $\sim 35\%$; (2) anastomosing
539 foliation and S-C fabrics (Figs. 6 and 7), (3) widespread presence of Dauphiné twinning
540 (Fig. 12) and; (4) kinematic indicators mostly consistent with sinistral sense of shear
541 (Figs. 5, 6, 7 and 8). The composite quartz microstructures, which include (partially
542 recrystallized) ribbons and grains, and matrix constituted of very fine-recrystallized
543 grains, observed in most thin sections, are well documented in the literature for quartz
544 deforming under greenschist conditions (e.g. Kjöll et al., 2015; Ceccato et al., 2017).

545 Quartzites and mylonite from G1 display old grains surrounded by smaller (~ 10
546 μm) recrystallized grains, mainly along serrated grain boundaries in quartz (Fig. 7h),
547 and also along fractures in feldspar (Fig. 7g). This points to BLG (Fig. 13a) as the main
548 dynamic recrystallization mechanism responsible for the intense grain-size reduction
549 process, indicating temperature conditions around 400 $^{\circ}\text{C}$ (e.g. Schmid and Handy,
550 1991; Stipp et al., 2002b). In the case of feldspar from the mylonite, the small
551 recrystallized grains could also be the result of classical nucleation, but differentiating
552 whether these grains are the product of recrystallization by BLG or by classical
553 nucleation is difficult, since both processes involve boundary migration (e.g. Fitz
554 Gerald and Stünitz, 1993). Both classical nucleation and recrystallization by BLG,
555 however, may occur at temperatures below 450 $^{\circ}\text{C}$ (e.g. Fitz Gerald and Stünitz, 1993),
556 and given the presence of the hydrated assemblage in the mylonite ($\sim 10\%$ of mica),
557 which may enhance these processes, dynamic recrystallization of feldspar together with
558 quartz is likely. Additionally, the presence of few quartz new grains with sizes close to
559 the subgrains (Fig. 7e) suggests that quartzite (LC59) was also recrystallized by SGR to
560 some extent.

561 Schists from G2 show S-C fabrics (Figs. 5b and c), garnet porphyroblasts with
562 recrystallized quartz in pressure shadows, and biotite fish, all suggestive of sinistral

563 shear (Figs. 6 and 8). The schists also have aggregates of deformed plagioclase that
 564 exhibit deformation twins (Figs. 8e and f), quartz recrystallized grains with sizes up to
 565 ~200 μm , with 50 to 85% of grains up to 50 μm in diameter (being ~25% >10-20 μm)
 566 in the EBSD mapped area, and significant evidence of SGR and GBM recrystallization
 567 (Figs. 13c, d, e, f). This evidence suggests that during sinistral shear-related dynamic
 568 recrystallization, rocks from G2 recrystallized by BLG and SGR, which lead to a
 569 decrease in grain-size, and by GBM, which lead to an increase in size of the
 570 recrystallized quartz grains, likely under higher temperature conditions (>400 – 500 $^{\circ}\text{C}$;
 571 e.g. Stipp et al., 2002b) than the deformation recorded by the G1 rocks.



572

573 **Figure 13** - Photomicrographs of the mylonitic granite (sample LC64B) from G1 and quartz schist from
 574 G2 (samples LC30DSC and LC30C1), and corresponding sketches displaying the main aspects of the
 575 intense recrystallization process. (a) and (b) Bulges and recrystallized small grains along the parent grain
 576 boundaries, indicating dominance of BLG recrystallization in the southern Lancinha shear zone. (c) and
 577 (d) subgrain boundaries oriented oblique to the foliation, suggesting SGR recrystallization and a slight
 578 temperature increase northwards along the Lancinha shear zone. (e) and (f) Irregular lobate grain
 579 boundaries and irregular amoeboid grain shapes suggesting GBM recrystallization and higher
 580 temperatures in the northern Lancinha shear zone.

581

582

583

584 The occurrence of BLG recrystallization in rocks displaying evidence for
 585 operation of both SGR and GBM, suggests that rocks from G2 were first deformed at
 586 higher temperature conditions and later underwent lower temperature deformation,
 587 given that BLG recrystallization is not expected to occur under the same high
 588 temperatures at which GBM operates (e.g. Platt and Behr, 2011). Therefore, GBM
 589 likely represents an older preserved microfabric overprinted by a later BLG during
 exhumation. Such an overprinting relationship is common in large-scale shear zones

590 with long-lasting deformation history (e.g. Means, 1995). BLG overprint on rocks first
591 recrystallized by GBM has also been suggested by Faleiros et al. (2011) for residual
592 neosones and mylonitic granitic leucosome (samples 137, 122 and 257 in their Figure 3
593 and Table 1) deformed close to the sinistral Serra do Azeite shear zone.

594 Schists with similar composition to the G2 schists immediately south of the town
595 of Barra do Turvo, between the Putunã and Serra do Azeite shear zones, were
596 recrystallized by GBM or both SGR and GBM (samples FM138, FM136 and 070 in
597 Figure 3 and Table 1 in Faleiros et al., 2011). Furthermore, considering the suggested
598 recrystallization mechanisms operating during quartz recrystallization in the whole area
599 studied by Faleiros et al. (2011), and the ones suggested here for the G2 rocks, a
600 competition between SGR and GBM mechanisms, with some secondary overprint by
601 BLG, seems to be a realistic scenario during dynamic recrystallization associated with
602 the deformation in the northern of the LSZ, and at the Putunã and Serra do Azeite shear
603 zones. Such a scenario implies similar deformation conditions for rocks deformed along
604 these shear zones.

605 Texture analysis results, such as the strong concentration of $\langle c \rangle$ axes close to
606 the Z direction (pole to foliation) plus the concentration of $\langle a \rangle$ axes parallel to X
607 (stretching lineation) suggest that the basal $\langle a \rangle$ slip is the dominant slip system in the
608 G1 quartzites LC09H and LC59 (Fig. 9). This slip system is typical for quartzites
609 deforming under low-temperature conditions (e.g. Schmid and Casey, 1986; Hirth and
610 Tullis, 1992; Stipp et al., 2002a), due to low-temperature dislocation creep (dislocation
611 glide) deformation mechanisms (e.g. Hirth and Tullis, 1992). Evidence for dislocation
612 creep in these rocks are intracrystalline deformation features such as undulose
613 extinction, subgrain boundaries and deformation bands. Dislocation glide was certainly
614 facilitated by intense dynamic recrystallization, given that under low temperature
615 conditions, dislocation glide can only accommodate a small amount of strain before
616 strain hardening and stress concentration lead to fracture (Davis et al., 2012). The
617 asymmetric distribution of $\langle c \rangle$ axes (at $\sim 30^\circ$ counterclockwise from Z) indicates
618 sinistral sense of shear and accommodation of non-coaxial deformation in the quartzites.
619 Subsidiary deformation by slip on the system rhomb $\langle a \rangle$ may also have occurred, as
620 there is some concentration of poles to $\{r\}$ close to Z, also confirmed in the IPFs maps
621 (e.g. Toy et al., 2008). It is difficult to infer slip systems from quartz texture in the
622 mylonitic granite (sample LC64B), and we can only mention that during strain
623 localization $\{z\}$ planes were oriented favorable for sliding. However, the presence of

624 some high-angle boundaries in the interval between >15 and 100° in the misorientation
625 angle histograms for this sample (Fig. 12) suggests a transition from dislocation creep to
626 dislocation accommodated grain boundary sliding (e.g. Miranda et al., 2016) or,
627 alternatively, a transition from dislocation creep to fluid assisted (or dissolution-
628 precipitation creep assisted) grain boundary sliding (e.g. Lagoeiro & Fueten, 2008), as
629 recrystallization, irrespective of its mechanisms, would not produce such a wide range
630 of angle distribution (Vernooij et al., 2006).

631 Small circles defined by quartz $\langle c \rangle$ axes are slightly oblique to Z in a
632 counterclockwise sense (samples LC30DSC Area 1 and Area 2 and LC30C1 Area 2),
633 suggesting activation of basal $\langle a \rangle$ slip and sinistral sense of shear (Fig. 9). Sinistral
634 sense of shear can also be extracted from $\langle c \rangle$ axis distribution from sample LC30C1
635 Area 1. However, textural analysis for this sample shows quartz $\langle c \rangle$ axes distributed
636 along a single girdle, which suggests a combination of multiple slip systems such as
637 basal + rhomb along the $\langle a \rangle$ direction. Combined activity of basal $\langle a \rangle$ and rhomb $\langle a \rangle$
638 slip systems can also be inferred from quartz $\langle c \rangle$ axis fabric and IPFs from sample
639 LC30C1 Area 3, and of rhomb $\langle a \rangle$ and prism $\langle a \rangle$ from the sample LC30C1 large area
640 map, which has a concentration of $\langle c \rangle$ axis around the center of the pole figure (Fig.
641 10). Nevertheless, the $\langle c \rangle$ axis distribution along a broad single girdle skewed $\sim 20^\circ$
642 clockwise with respect to Z in the LC30C1 Area 3 suggests local dextral sense of shear,
643 while a more symmetric distribution in the LC30C1 large area map can be related to a
644 coaxial component of deformation. These observations point to strain partitioning at the
645 sample scale during overall non-simple shear (e.g. transpressional) deformation.
646 Furthermore, the presence of subgrain boundaries give microstructural evidence for
647 crystal-plastic deformation (Passchier and Trouw, 2005), and suggests that the
648 activation of multiple slip systems is due to dislocation creep deformation mechanism,
649 likely involving dislocation climb at moderate temperature conditions. Dislocation
650 creep deformation mechanism is also supported by the evidence of intracrystalline
651 deformation in biotite, amphibole and plagioclase (Fig. 8).

652 All together, these data suggest that strain localization during the development of
653 the Lancinha and associated shear zones was facilitated by intense grain-size reduction,
654 as observed in many other shear zones elsewhere (e.g. Lloyd 2004; Menegon et al.,
655 2010; Platt and Behr, 2011). More specifically, while BLG is the dominating grain-size
656 reducing mechanism in the southern region (G1 rocks), in the northern region (G2
657 rocks) SGR contributes significantly to the grain-size reduction process. In the northern

658 region, GBM also might have contributed to the strain localization. Strain localization
659 was certainly also facilitated by the pervasive development of Dauphiné twinning, as
660 the presence of such twins reduces the strength of quartz and contributes to the grain-
661 size reduction process (e.g. Lloyd, 2004; Stipp and Kunze, 2008; Menegon et al., 2010).
662 This recrystallization evidence, the dominant asymmetry of $\langle c \rangle$ axis orientation
663 observed in rock from both groups, plus the mainly activation of basal $\langle a \rangle$ slip in the
664 southern region, and the combination of basal $\langle a \rangle$ + rhomb $\langle a \rangle$ + prism $\langle a \rangle$ in the
665 northern region, is consistent with the interpretation presented above that strain
666 localization occurred under temperatures of ~ 400 °C in the southern part and between
667 $>400 - 500$ °C in the northern region, and involved a strong non-coaxial sinistral
668 component during plastic deformation of the whole studied shear zone segment. It is
669 worth noting that the suggestion of a slight increase in temperature towards the north of
670 the LSZ is based on microstructural observations, mineral assemblage (biotite, K-
671 feldspar, plagioclase, garnet, amphiboles in the north), and EBSD data from both group
672 samples, and not only on the crystallographic fabrics. The crystallographic fabrics of
673 sample LC30C1 from G2 show $\langle c \rangle$ axis distributed along girdles, some of them with
674 maxima around Y. Such crystallographic fabrics, which suggest activation of
675 rhombohedral and prismatic forms, could also result from a higher strain condition (e.g.
676 Pennacchioni et al., 2010), as the temperature dependence for sliding along direction
677 $\langle a \rangle$ has not been convincingly demonstrated (e.g. Kilian and Heilbronner, 2017).
678 However, since we do not have any single Y maxima of $\langle c \rangle$ axis in our samples, a
679 temperature of 500 °C seems to be a realistic maximum temperature estimate for
680 deformation in the entire studied segment of the LSZ, given that the transition from
681 combined basal, rhomb and prism $\langle a \rangle$ slip to dominant prism $\langle a \rangle$ slip, i.e. from YZ
682 girdle distributions to $\langle c \rangle$ axis Y maximum, likely occurs at 500 °C (Stipp et al.,
683 2002a).

684 In summary, microstructural observations and textural analysis suggest that
685 rocks from G1 recrystallized mainly by BLG and were deformed under temperature
686 ~ 400 °C, with activation of basal $\langle a \rangle$ slip system. On the other hand, rocks from G2
687 likely recrystallized by SGR and GBM (with some later BLG recrystallization), and
688 were deformed at $>400 - 500$ °C, with activation of multiple slip systems (basal $\langle a \rangle$,
689 rhomb $\langle a \rangle$ and prism $\langle a \rangle$). Rocks from G1 in comparison with rocks from G2 have a
690 higher amount of grains smaller than 50 μm , and are associated with strongly fractured
691 feldspar with recrystallized grains along its fractures and margins. Rocks from G2 have

692 larger amounts of recrystallized grains with sizes up 200 μm and are associated with
693 plagioclase with deformation twins, and plastically deformed amphibole and biotite.
694 The different microstructures, deformation mechanisms and temperatures show that the
695 way these different rocks responded to deformation varied widely during the shear zone
696 evolution. Such a variance could be due to differences in the amount of exhumation, the
697 north portion of the studied segment representing a slightly deeper section through the
698 LSZ. Alternatively, deformation may have continued for somewhat longer in the south
699 during exhumation-related cooling. More microstructural data, especially in the south
700 portion of LSZ, in combination with geochemical and geochronological analysis are
701 necessary to better evaluate these alternatives.

702

703 5.2. Implications for the tectonic evolution of the Ribeira belt

704

705 The tectonic evolution of the southern Ribeira belt, principally concerning the
706 Curitiba terrain, has recently been interpreted as the result of a polyphase deformation
707 history with six successive phases of deformation occurring from 600 to 580 Ma, with
708 three of these (D3-D6) developing over a time period of only four million years (584-
709 580 Ma; Faleiros et al., 2016). This interpretation was based on inclusions pattern in
710 porphyroblasts (D1-D2) predated by the main foliation (D3), and mesoscopic to
711 regional folding of the main foliation (D4-D5) with folds being flanked by shear zones
712 (D6). Considering that we are dealing with an anastomosing interconnected shear zone
713 system at a large-orogenic scale, with geometric complexities at a variety of scales, we
714 would argue that much if not all of this deformation history may be the result of
715 progressive orogenic deformation (e.g. Fossen et al., 2019). In this regard, Faleiros et al.
716 (2016) also indicate that some of their six deformation phases could represent
717 progressive deformation.

718 Another characteristic feature of many transpressional orogenic sections is the
719 tendency for strain to partition into pure shear-dominated domains separated by strike-
720 slip (dominated) shear zones that accommodate much or all of the simple shear
721 displacement (e.g. Oldow, 1990; Tikoff and Teyssier, 1994). In many cases strain
722 partitioning becomes more pronounced at late stages of deformation, and the
723 progressive localization of shear into shear zones (D6 of Faleiros et al., 2016) could
724 work in tandem with shortening by thrusting and folding (D4-D5) in the pure shear-
725 domains between the shear zones. Such partitioned transpressional (and locally

726 transtensional) deformation has been suggested further north, from geometrical
727 construction along the Serra do Azeite shear zone in the Apiaí terrain (Dehler et al.,
728 2007), and along the Taxaquara shear zone (Ribeiro et al., 2019), and for the Ribeira
729 belt as a whole (Ebert and Hasui, 1998).

730 The above-mentioned strain partitioning occurs at the scale of tens of kilometers,
731 but we also observe structural features that can be related to strain partitioning at
732 smaller scales. The partitioning relates to rheologic differences down to the microscale,
733 where micaceous layers behave different from quartzo-feldspatic layers. S-C structures
734 are a particularly common type of small-scale strain partitioning structure, and
735 microstructures also reveal differences in type of deformation or flow. While several
736 samples show consistent sinistral flow, quartz-schists from G2 display quartz texture
737 mainly suggestive of sinistral shear, but with a local more symmetric distribution and
738 even an observation of local dextral sense of shear, as inferred from quartz *c* axis
739 distributions (Fig. 10). This may be a microscale example of partitioning of
740 transpression, where the pure shear component produces conjugate shear bands.
741 Alternatively, such partitioning can be set up by local rheologic or geometric
742 irregularities that produce local non-laminar flow, by slip on foliations (Harris and
743 Cobbold, 1984) and by temporal flow variations (Hudleston, 1999). Common for all of
744 these expressions of strain partitioning is that they would become more pronounced
745 over time, as heterogeneities such as steep fold limbs and foliations develop. On a large
746 scale, linkage of shear zone segments to form the observed anastomosing framework
747 creates spatial variations in flow. Interestingly, similar patterns are seen at the
748 microscale, where anastomosing patterns of phyllosilicates surround more quartzo-
749 feldspatic lenses (Figs. 6b and 7c).

750 The consistent sinistral sense of shear found in this work contrasts with the
751 dextral sense of shear loosely assigned to the Lancinha shear zone by previous workers
752 (e.g. Faleiros et al., 2010, 2011, 2016). However, we have not been able to find actual
753 evidence in support of such dextral sense of shear in the published literature. Unlike the
754 dextral Ribeira shear zone to the northwest (Fig. 3), which exhibits clockwise rotation
755 of foliation and lithologic contacts into the shear zone consistent with dextral shear, the
756 Lancinha shear zone shows no such rotations clear enough to reveal its sense of shear.
757 Hence, we will depart from the outcrop and microscale observations of sinistral sense of
758 shear presented here.

759 The observed kinematics of the Lancinha shear zone conforms with the sinistral
760 shear assigned to the Putunã and Serra do Azeite shear zones to the southeast (Fig. 2;
761 Dehler et al., 2007; Faleiros et al. 2011, 2016). These two sinistral shear zones parallel
762 the Lancinha shear zone, while the Ribeira shear zone to the northwest has a more
763 easterly trend (Fig. 3). The difference in orientation ($\sim 20^\circ$) between the dextral Ribeira
764 and the sinistral Lancinha, Putunã and Serra do Azeite shear zones is lower than what
765 would be expected for a conjugate set, even when considering that in a transpressional
766 setting, the pure shear component would lower the angle somewhat over time. Hence,
767 we are probably facing a more complex kinematic picture that could in part be caused
768 by kinematic complications along a composite anastomosing shear zone network
769 affecting a rheologically heterogeneous portion of the crust. Lateral extrusion or escape
770 of blocks between shear zones of similar orientations has been suggested (Faleiros et al.,
771 2010, 2016). Lateral escape has also been discussed from many other orogenic belts
772 worldwide, and this may be a feasible explanation for subparallel shear zones showing
773 opposite kinematics. In the well-explored case of the Himalayan-Tibetan system, lateral
774 escape or extrusion is generally explained in terms of indenter tectonics, with the old
775 and rigid Indian crust representing a more rigid block than the Asian crust (e.g. Molnar
776 and Tapponnier, 1975). In this context, we speculate that the Congo craton might
777 represent such an indenter relative to a softer Brasilia-belt crust on the west side of the
778 southern Ribeira belt.

779 Eroded sections through regions of extrusion tectonics settings are identified in
780 several ancient orogenic settings, including the Paleoproterozoic Superior boundary
781 zone in Canada (Kuiper et al., 2011), the Neoproterozoic of NE Brazil (Borborema
782 Province; Araujo et al., 2014) and East Africa-Antarctica (Jacobs and Thomas, 2004). A
783 particularly interesting and well-documented system is the Appalachian example
784 described by Massey and Moecher (2013). Also here, subparallel dextral and sinistral
785 shear zones unexpectedly coexist in an overall dextral transpressional orogenic setting.
786 Geochronologic constraints, metamorphic and textural observations and structural
787 relations demonstrate that the opposing shear senses and related structures were coeval.
788 Furthermore, variations in structural patterns show that deformation was partitioned in a
789 rather complex way, with zones of varying kinematic vorticity, lineation orientations
790 and strain patterns. In this Appalachian example, the progressive deformation lasted for
791 30 m.y. (330-300 Ma; Massey and Moecher, 2013). In the Ribeira belt, the relevant
792 deformation lasted for just a few million years (584-580; D3-D6 of Faleiros et al.,

793 2016), which would normally be taken to represent a single progressive deformation.
 794 Hence, it is reasonable to assume that the dextral and sinistral deformation represented
 795 by the shear zones in this region were coeval as well.

796 According to previous workers (Passarelli et al, 2011; Faleiros et al., 2011,
 797 2016) the sinistral shear sense on the Lancinha shear zone is replaced by dextral shear to
 798 the northeast, in the segment known as the Cubatão shear zone. This could be related to
 799 dextral shear being taken up by the adjoining Ribeira shear zone, meaning that the block
 800 between the Ribeira and the Lancinha shear zones was extruding southwestward, as
 801 illustrated in Figure 14. The result of such a progressive extrusion would be a zipper-
 802 style merging of the Ribeira and Lancinha shear zones as the extrusion proceeds, and
 803 possibly with a southwestward increasing effect of extrusion. More targeted kinematic
 804 analysis and deformation dating along the different segments of this intriguing shear
 805 zone system is needed to evaluate this model.

806

807

808

809

810

811

812

813

814

815

816

817

818

819

820

821

822

823

824

825

826

827

828

829

830

831

832

833

834

835

836

837

838

839

840

841

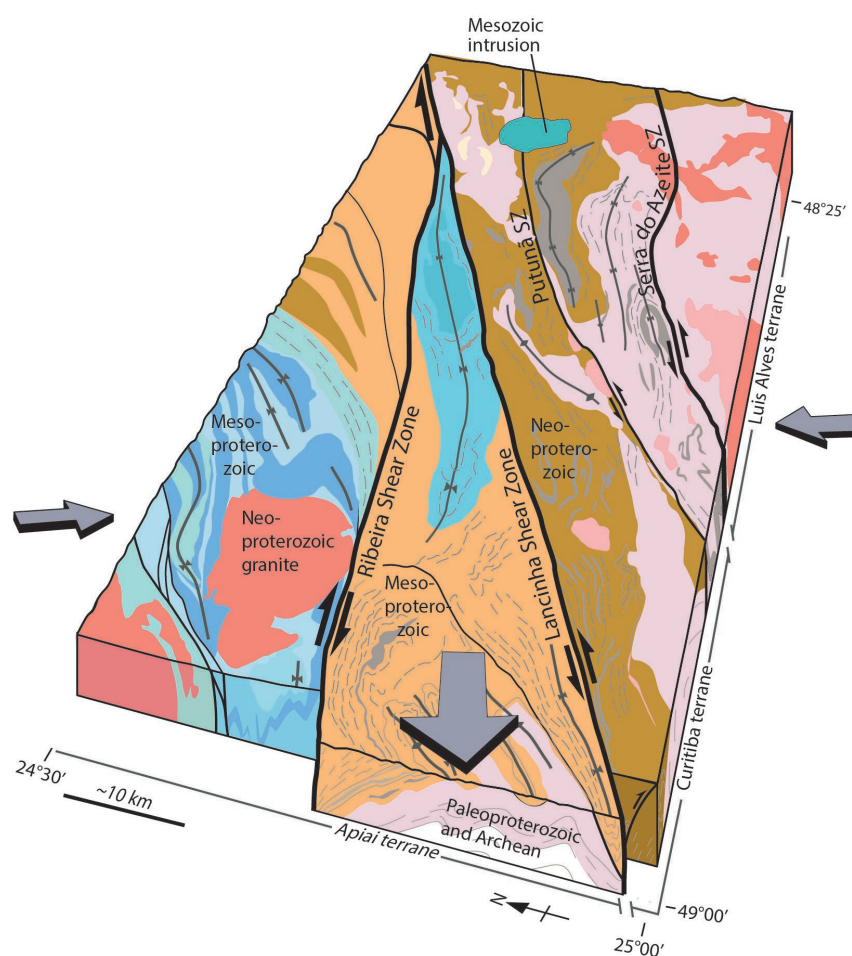


Figure 14 – Block diagram illustrating the southwestward escape of the block bounded by the Ribeira and Lancinha shear zones during transpressive orogenic shortening. Modified from Fossen et al. (2019). Colors roughly corresponding to Fig. 3.

6. CONCLUSIONS

We have performed a detailed structural mapping and microstructural study and applied the SEM-ESBD technique to analyze the full crystallographic orientation of quartz grains in quartzites, mylonitic granite and quartz-schists that were intensely recrystallized during the development of the Lancinha Shear Zone in the anastomosing southern Ribeira belt shear zone system. Our study shows that:

- 1- Rocks were intensely recrystallized by BLG, especially in the southern portion of the Lancinha Shear Zone, and also by SGR and GBM in the northern portion. BLG and SGR seem to be the main recrystallization mechanisms responsible for grain-size reduction;
- 2- The plastic deformation along the LSZ is accommodated mainly by dislocation creep, with activation of basal $\langle a \rangle$ in the southern region and rhomb $\langle a \rangle$ + basal $\langle a \rangle$ and prism $\langle a \rangle$ in the northern region. The strain localization was facilitated by dynamic recrystallization due to BLG, SGR and GBM recrystallization, under temperature conditions at around 400 °C in the southern region, and at around >400 to 500 °C in the northern region, and by pervasive Dauphiné twinning;
- 3- The anastomosing pattern defined by interconnected shear zones observed at meso- and macroscale (Figs. 2 and 5) is also identified at the microscale by the occurrence of S-C foliation and anastomosing foliation associated with flattened quartz grains (Figs. 6 and 7);
- 4- The analysis of a broad variation of shear sense indicators, such as biotite fish, S-C fabrics and rotated porphyroblasts, indicate predominantly sinistral sense of shear on the LSZ. This is also inferred from quartz $\langle c \rangle$ axis distribution, which have asymmetric girdles rotated counterclockwise to Z;
- 5- Our observations fit a general model for an overall dextral transpressional system for the Ribeira belt that involves lateral extrusion and dual sense of shear on shear zones, bounding extruding blocks during a progressive orogenic evolution.
- 6- The predominance of sinistral kinematic indicators, different from what has been superficially suggested in the recent literature (e.g. Faleiros et al., 2016), suggests that interpretation on kinematics and, consequently, tectonic evolution of such interconnected shear zone systems should be done with

876 great care, especially in transpressional regimes involving strain partitioning.
 877 Further investigation involving dating of the plastic deformation is needed to
 878 better understand the significance of such a sinistral shear in an overall
 879 dextral orogenic setting.

880

881

882 **ACKNOWLEDGMENTS**

883

884 TC wishes to thank the Coordenação de Aperfeiçoamento de Pessoal de Nível
 885 Superior-Brasil (CAPES) for the granting of the master's scholarship (Finance code
 886 001). This work was partially funded by the Brazilian National Council for research and
 887 Technology Development (CNPq) via processes number 434202/2018-5 to CC, and
 888 305232/2018-5 and 425412/2018-0 to LL. The manuscript was greatly benefited by the
 889 reviews of Alberto Ceccato and an anonymous reviewer. We are also grateful to
 890 Rheinhardt Fuck for careful editorial handling. We would like to thank Gustavo Viegas
 891 and Rhander Altoé, whose contributions helped to improve this work, and Rodrigo
 892 Santos for field assistance.

893

894 **REFERENCES**

895

896 Araujo, C.E.G., Weinberg, R., Cordani, U., 2013. Extruding the Borborema Province
 897 (NE-Brazil): a two-stage Neoproterozoic collision process. *Terra Nova*, 26, 157-
 898 168. <https://doi.org/10.1111/ter.12084>

899

900 ASTM E2627-13 (2019), Standard Practice for Determining Average Grain Size Using
 901 Electron Backscatter Diffraction (EBSD) in Fully Recrystallized Polycrystalline
 902 Materials, ASTM International, West Conshohocken, PA, 2019.

903

904 Bachmann, F., Hielscher, R., Schaeben, H., 2010. Texture Analysis with MTEX - Free
 905 and Open Source Software Toolbox. *Solid State Phenomena*, 160, 63-68.
 906 <https://doi.org/10.4028/www.scientific.net/SSP.160.63>

907 Bento dos Santos, T., Tassinari, C., Fonseca, P., 2015. Diachronic collision, slab break-
 908 off and long-term high thermal flux in the Brasiliano-Pan-African orogeny:
 909 implications for the geodynamic evolution of the Mantiqueira Province.
 910 *Precambrian Research*, 260, 1–22.
 911 <https://doi.org/10.1016/j.precamres.2014.12.018>

912 Berger, A., Herwegh, M., Schwarz, J.O., Putlitz, B., 2011. Quantitative analysis of
 913 crystal/grain sizes and their distributions in 2D and 3D., *Journal of Structural*
 914 *Geology*. <https://doi.org/10.1016/j.jsg.2011.07.002>

- 915
916 Campagnoli, F., 1996. Considerações sobre a geologia da sequência Turvo-Cajati, na
917 região do alto Rio Jacupiranguinha, SP. Inst. De Geociências, Universidade de
918 São Paulo, São Paulo, Dissertação de Mestrado, 93p.
919
- 920 Campanha, A.G.C., 2002. O papel do sistema de zonas de cisalhamento transcorrentes
921 na configuração da porção meridional da Faixa Ribeira. Tese de Livre Docência,
922 Universidade de São Paulo. [https://doi.org/10.11606/T.44.2009.tde-16122009-
923 094247](https://doi.org/10.11606/T.44.2009.tde-16122009-094247)
924
- 925 Campanha, G.A.C., Faleiros, F.M., Basei, M.A.S., Tassinari, C.C.G., Nutman, A.P.,
926 Vasconcelos, P.M., 2015. Geochemistry and age of mafic rocks from the
927 Votuverava Group, southern Ribeira belt, Brazil: Evidence for 1490 Ma oceanic
928 back-arc magmatism. *Precambrian Research*, 266, 530–550.
929 <https://doi.org/10.1016/j.precamres.2015.05.026>
930
- 931 Cavalcante, C., Lagoeiro, L., Fossen, H., Egydio-Silva, M., Morales, L.F.G., Ferreira,
932 F., Conte, T., 2018. Temperature constraints on microfabric patterns in
933 quartzofeldspathic mylonites, Ribeira belt (SE Brazil). *Journal of Structural
934 Geology*, 115, 243-262. <https://doi.org/10.1016/j.jsg.2018.07.013>
935
- 936 Ceccato, A., Pennacchioni, G., Menegon, L., Bestmann, M., 2017. Crystallographic
937 control and texture inheritance during mylonitization of coarse grained quartz
938 veins. *Lithos* 290-291. <https://doi.org/10.1016/j.lithos.2017.08.005>
939
- 940 Davis, G.H., Reynolds, S.J., Kluth, C., 2012. *Structural Geology of Rocks and Regions*.
941 3rd edition. 861p.
942
- 943 Dehler, N.M., Machado, R., Vasconcelos, C.S., 2000. Tectônica extensional oblíqua no
944 sul do Estado de São Paulo. *Rev. Brasileira de Geociências*, 30, 699-706.
945
- 946 Dehler, N.M., Machado, R., Fassbinder, E., 2007. Shear structures in the Serra do
947 Azeite Shear Zone, southeastern Brazil: transtensional deformation during
948 regional transpression in the central Mantiqueira province (Ribeira Belt). *Journal
949 of South America Earth Sciences*, 23, 176-192.
950 <https://doi.org/10.1016/j.jsames.2006.09.017>
951
- 952 Ebert, H.D., Hasui, Y., 1998. Transpressional tectonics and strain partitioning during
953 oblique collision between three plates in the Precambrian of southeast Brazil. In:
954 Holdsworth, R.E., Strachan, R.A. (Eds.), *Continental Transpressional and
955 Transtensional Tectonics*. Geology Society, London, Special Publications, 135,
956 231-252. <https://doi.org/10.1144/GSL.SP.1998.135.01.15>
957
- 958 Faleiros, F.M., Campanha, G.A.C., Bello, R.M.S., Fuzikawa, K., 2010. Quartz
959 recrystallization regimes, c-axis texture transitions and fluid inclusion
960 reequilibration in a prograde greenschist to amphibolite facies mylonite zone
961 (Ribeira Shear Zone, SE Brazil). *Tectonophysics*, 485, 193–214.
962 <https://doi.org/10.1016/j.tecto.2009.12.014>
963

- 964 Faleiros, F.M., Campanha, G.A.C., Martins, L., Vlach, S.R.F., Vasconcelos, P.M.,
965 2011. Ediacaran high-pressure collision metamorphism and tectonics of the
966 southern Ribeira Belt (SE Brazil): evidence for terrane accretion and dispersion
967 during Gondwana assembly. *Precambrian Research*, 189, 263-291.
968 <https://doi.org/10.1016/j.precamres.2011.07.013>
969
- 970 Faleiros, F.M., Morais, S.M., Costa, V.S., 2012. Geologia e Recursos Minerais da Folha
971 Apiaí – SG.22-X-B-V – Estados de São Paulo e Paraná. CPRM- Serviço
972 Geológico do Brasil, Escala 1:100.000.
973
- 974 Faleiros F.M., and Pavan M., 2013. Geologia e Recursos Minerais da Folha Eldorado
975 Paulista – SG-22-X-B-XI, Estado de São Paulo. Companhia de Pesquisa de
976 Recursos Minerais, CPRM, Escala 1:100.000.
977
- 978 Faleiros, F.M., Campanha, G.A.C., Pavan, M., Almeida, V.V., Rodrigues, S.W.O.,
979 Araújo, B.P., 2016. Short-lived polyphase deformation during crustal thickening
980 and exhumation of a collisional orogen (Ribeira Belt, Brazil). *Journal of*
981 *Structural Geology*, 93, 106-130. <https://doi.org/10.1016/j.jsg.2016.10.006>
982
- 983 Fitz Gerald, J.D., and Stünitz, H. 1993. Deformation of granitoids at low metamorphic
984 grade. I: Reactions and grain size reduction. *Tectonophysics* 221, 269-297.
985 [https://doi.org/10.1016/0040-1951\(93\)90163-E](https://doi.org/10.1016/0040-1951(93)90163-E)
986
- 987 Fossen, H., Cavalcante, G.C.G., 2017. Shear Zones - A review. *Earth-Science Reviews*,
988 171, 434-455. <https://doi.org/10.1016/j.earscirev.2017.05.002>
989
- 990 Fossen, H., Cavalcante, G.C.G., Pinheiro, R.V., Archanjo, C.J., 2019. Deformation –
991 Progressive or Multiphase? *Journal of Structural Geology*, 125, 82-99.
992 <https://doi.org/10.1016/j.jsg.2018.05.006>
993
- 994 Harris, L.B., Cobbold, P.R., 1984. Development of conjugate shear bands during bulk
995 simple shearing. *Journal of Structural Geology*, 7, 37-44.
996 [https://doi.org/10.1016/0191-8141\(85\)90113-0](https://doi.org/10.1016/0191-8141(85)90113-0)
997
- 998 Heilbronner, R., Tullis, J., 2006. Evolution of c axis pole figures and grain size during
999 dynamic recrystallization: Results from experimentally sheared quartzite.
1000 *Journal of Geophysical Research*, 111, B10202.
1001 <https://doi.org/10.1029/2005JB004194>
1002
- 1003 Herwegh, M., 2000. A new technique to automatically quantify microstructures of fine
1004 grained carbonate mylonites: two step etching combined with SEM imaging and
1005 image analysis. *Journal of Structural Geology* 22, 391-400. [10.1016/S0191-](https://doi.org/10.1016/S0191-8141(99)00165-0)
1006 [8141\(99\)00165-0](https://doi.org/10.1016/S0191-8141(99)00165-0)
- 1007
- 1008 Hielscher, R., Schaeben, H., 2008. A novel pole figure inversion method: specification
1009 of the MTEX algorithm. *Journal of Applied Crystallography*, 41, 1024-1037.
1010 <https://doi.org/10.1107/S0021889808030112>
1011

- 1012 Hirth, G., Tullis, J., 1992. Dislocation creep regimes in quartz aggregates. *Journal of*
1013 *Structural Geology*, 14, 145-159. [https://doi.org/10.1016/0191-8141\(92\)90053-Y](https://doi.org/10.1016/0191-8141(92)90053-Y)
1014
- 1015 Hobbs, B., Mühlhaus, H.-B., Ord, A., 1990. Instability, softening and localization of
1016 deformation. *Geological Society, London, Special Publications*, 54(1), 143–165.
1017 <https://doi.org/10.1144/GSL.SP.1990.054.01.15>
1018
- 1019 Hudleston, P., 1999. Strain compatibility and shear zones: is there a problem? *Journal of*
1020 *Structural Geology*, 21, 923-932. [https://doi.org/10.1016/S0191-8141\(99\)00060-](https://doi.org/10.1016/S0191-8141(99)00060-7)
1021 [7](https://doi.org/10.1016/S0191-8141(99)00060-7)
1022
- 1023 Jacobs, J., Thomas, R.J., 2004. Himalayan-type indenter-escape tectonics model for the
1024 southern part of the late Neoproterozoic-early Palaeozoic East African-Antarctic
1025 orogen. *Geology*, 32, 721-724. <https://doi.org/10.1130/G20516.1>
1026
- 1027 James, D.E., Assumpção, M., 1996. Tectonic implications of S-wave anisotropy
1028 beneath SE Brazil. *Geophysical Journal International*, 126, 1-10.
1029 <https://doi.org/10.1111/j.1365-246X.1996.tb05263.x>
1030
- 1031 Kilian, R. and Heilbronner, R., 2017. Analysis of crystallographic preferred orientations
1032 of experimentally deformed Black Hills Quartzite. *Solid Earth*, 8, 1095-1117.
1033 <https://doi.org/10.5194/se-8-1095-2017>
1034
- 1035 Lagoeiro, L., Fueten, F., 2008. Fluid-assisted grain boundary sliding in bedding-parallel
1036 quartz veins deformed under greenschist metamorphic grade. *Tectonophysics*
1037 446, 42-50. <https://doi.org/10.1016/j.tecto.2007.10.004>
1038
- 1039 Lister, G. S., Paterson, M. and Hobbs, B. E., 1978. The simulation of fabric
1040 development during plastic deformation and its application to quartzite: the
1041 model. *Tectonophysics*, 45, 107–158. [https://doi.org/10.1016/0040-](https://doi.org/10.1016/0040-1951(78)90004-5)
1042 [1951\(78\)90004-5](https://doi.org/10.1016/0040-1951(78)90004-5)
1043
- 1044 Lister, G.S., Hobbs, B.E., 1980. The simulation of fabric development during plastic
1045 deformation and its application to quartzite: the influence of deformation history.
1046 *Journal of Structural Geology*, 2, 227-247. [https://doi.org/10.1016/0191-](https://doi.org/10.1016/0191-8141(80)90023-1)
1047 [8141\(80\)90023-1](https://doi.org/10.1016/0191-8141(80)90023-1)
1048
- 1049 Kuiper, Y.D., Lin, S., Böhm, C.O., 2011. Himalayan-type escape tectonics along the
1050 Superior Boundary Zone in Manitoba, Canada. *Precambrian Research*, 187, 248-
1051 262. <https://doi.org/10.1016/j.precamres.2011.03.009>
1052
- 1053 Kjöll, H.J., Viola, G., Menegon, L., Sørensen, B.E., 2015. Brittle-viscous deformation
1054 of vein quartz under fluid-rich lower greenschist facies conditions. *Solid Earth*.
1055 <https://doi.org/10.5194/se-6-681-2015>
1056
- 1057 Little, T.A., Hacker, B.R., Brownlee, S.J., Seward, G., 2013. Microstructures and quartz
1058 lattice-preferred orientations in the eclogite-bearing migmatitic gneisses of the
1059 D'Entrecasteaux Islands, Papua New Guinea. *Geochemistry, Geophysics,*
1060 *Geosystems*, 14, 2030-2062. <https://doi.org/10.1002/ggge.20132>
1061

- 1062 Lloyd, G.E., 2004. Microstructural evolution in a mylonitic quartz simple shear zone:
1063 the significant roles of dauphine twinning and misorientation. In: Alsop, G.I.,
1064 Holdsworth, R.E., McCaffrey, K.J.W., Hand, M. (Eds.), Flow processes in faults
1065 and shear zones. Geological Society of London, Special Publications, 224, 39–
1066 61. <https://doi.org/10.1144/GSL.SP.2004.224.01.04>
1067
- 1068 Machado, R., Dehler, N.M., Vasconcelos, P., 2007. $^{40}\text{Ar}/^{39}\text{Ar}$ ages (600-570 Ma) of the
1069 Serra do Azeite transtensional shear zone: evidence for syncontractual
1070 extension in the Cajati area, southern Ribeira belt. Anais da Academia Brasileira
1071 de Ciências 79, 713–723. <http://dx.doi.org/10.1590/S0001-37652007000400011>
1072
- 1073 Machado, R., Philipp, R.P., McCreath, I., Peucat, J.J., 2016. Geochemical and isotopic
1074 evidence for the petrogenesis and emplacement tectonics of the Serra dos Órgãos
1075 batholith in the Ribeira Belt, Rio de Janeiro, Brazil. Journal of South America
1076 Earth Sciences, 68, 187–204. <https://doi.org/10.1016/j.jsames.2016.01.005>
1077
- 1078 Mancktelow, N.S., Pennacchioni, G., 2004. The influence of grain boundary fluids on
1079 the microstructure of quartz-feldspar mylonites. Journal of Structural Geology,
1080 26, 47-69. [https://doi.org/10.1016/S0191-8141\(03\)00081-6](https://doi.org/10.1016/S0191-8141(03)00081-6)
1081
- 1082 Massey, M.A., Moecher, D.P., 2013. Transpression, extrusion, partitioning, and lateral
1083 escape in the middle crust: Significance of structures, fabrics, and kinematics in
1084 the Bronson Hill zone, southern New England, U.S.A. Journal of Structural
1085 Geology, 55, 62-78. <https://doi.org/10.1016/j.jsg.2013.07.014>
1086
- 1087 Means, W., 1995. Shear zones and rock history. Tectonophysics, 247, 157-160.
1088 [https://doi.org/10.1016/0040-1951\(95\)98214-H](https://doi.org/10.1016/0040-1951(95)98214-H)
1089
- 1090 Menegon, L., Piazzolo, S., Pennacchioni, G., 2010. The effect of Dauphiné twinning on
1091 plastic strain in quartz. Contributions to Mineralogy and Petrology, 161, 635-
1092 652. <https://doi.org/10.1007/s00410-010-0554-7>
1093
- 1094 Miranda, E.A., Hirth, G., John, B.E., 2016. Microstructural evidence for the transition
1095 from dislocation creep to dislocation-accommodated grain boundary sliding in
1096 naturally deformed plagioclase. Journal of Structural Geology, 92, 30-45.
1097 <https://doi.org/10.1016/j.jsg.2016.09.002>
1098
- 1099 Molnar, P., Tapponnier, P., 1975. Cenozoic tectonics of Asia: Effects of a continental
1100 collision. Science, 189 (4201), 419-426.
1101 <https://doi.org/10.1126/science.189.4201.419>
1102
- 1103 Neumann, B., 2000. Texture development of recrystallised quartz polycrystals
1104 unravelled by orientation and misorientation characteristics. Journal of Structural
1105 Geology, 22, 1695-1711. [https://doi.org/10.1016/S0191-8141\(00\)00060-2](https://doi.org/10.1016/S0191-8141(00)00060-2)
1106
- 1107 Oldow, J.S., 1990. Transpression, orogenic float, and lithospheric balance. Geology, 18,
1108 991-994. [https://doi.org/10.1130/0091-613\(1990\)018<0991:TOFALB>2.3.CO;2](https://doi.org/10.1130/0091-613(1990)018<0991:TOFALB>2.3.CO;2)
1109
- 1110 Passareli, C. R., Basei, M. A. S., Wemmer, K., Sigajr, O., Oyhantçabal, P., 2011. Major
1111 shear zones of southern Brazil and Uruguay: escape tectonics in the eastern

- 1112 border of Rio de La plata and Paranapanema cratons during the Western
 1113 Gondwana amalgamation. *International Journal of Earth Sciences*, 100(2-3),
 1114 391-414. <https://doi.org/10.1007/s00531-010-0594-2>
 1115
- 1116 Passchier, C., Trouw, R. A., 2005. *Microtectonics*, 2nd edition. ISBN 978-3-540-29359-
 1117 0.
 1118
- 1119 Platt, J.P., and Behr, W., 2011. Grainsize evolution in ductile shear zones: Implications
 1120 for strain localization and the strength of the lithosphere. *Journal of Structural*
 1121 *Geology*, 33, 537-550. <https://doi.org/10.1016/j.jsg.2011.01.018>
 1122
- 1123 Pennacchioni, G., Menegon, L., Leiss, B., Nestola, F., and Bromiley, G., 2010.
 1124 Development of crystallographic preferred orientation and microstructure during
 1125 plastic deformation of natural coarse- grained quartz veins, *J. Geophys. Res.-Sol.*
 1126 *Ea.*, 115, B12. <https://doi.org/10.1029/2010JB007674>, 2010
 1127
- 1128 Poirier, J.P., 1980. Shear localization and shear instability in materials in the ductile
 1129 field. *Journal of Structural Geology*, 2, 135-142. [https://doi.org/10.1016/0191-
 1130 8141\(80\)90043-7](https://doi.org/10.1016/0191-8141(80)90043-7)
 1131
- 1132 Price, G. P. 1985. Preferred orientations in quartzites. In: Wenk, H. R. (ed.) *Preferred*
 1133 *Orientation in Deformed Metals and Rocks: An Introduction to Modern Texture*
 1134 *Analysis*. Academic Press, Inc., Orlando, 385–406.
 1135 <http://hdl.handle.net/102.100.100/276454?index=1>
 1136
- 1137 Ramsay, J.G., 1980. Shear zone geometry: a review. *Journal of Structural Geology*,
 1138 2(½), 83-99. [https://doi.org/10.1016/0191-8141\(80\)90038-3](https://doi.org/10.1016/0191-8141(80)90038-3)
 1139
- 1140 Ribeiro, T.B.V., Faleiros, F.M., Campanha, G.A.C., Lagoeiro, L., Weinberg, R.F.,
 1141 Hunte, N.J.R., 2019. Kinematics, nature of deformation and tectonic setting of
 1142 the Taxaquara Shear Zone, a major transpressional zone of the Ribeira Belt (SE
 1143 Brazil). *Tectonophysics*, 751, 83–108.
 1144 <https://doi.org/10.1016/j.tecto.2018.12.025>
 1145
- 1146 Sadowski, G.R., 1991. A megafalha de Cubatão no Sudeste Brasileiro. *Boletim IG-*
 1147 *USP. Serie Científica*, 22, 15-28. [https://doi.org/10.11606/issn.2316-
 1148 8986.v22i0p15-28](https://doi.org/10.11606/issn.2316-8986.v22i0p15-28)
 1149
- 1150 Schmid, S.M., Casey, M., 1986. Complete fabric analysis of some commonly observed
 1151 quartz c-axis patterns. *Geophysical Monograph Series*, 36, 263-286.
 1152 <https://doi.org/10.1029/GM036p0263>
 1153
- 1154 Schmid, S.M., Handy, M.R., 1991. Towards a genetic classification of fault rocks:
 1155 geological usage and tectonophysical implications. In: Moller, D.W., Mckenzie,
 1156 J.A., Weissert, H. (Eds), *Controversies in Modern Geology*. Academic Press,
 1157 London, 339-361.
 1158
- 1159 Stipp, M., Stünitz, H., Heilbronner, R., Schmid, S.M., 2002a. The eastern Tonale fault
 1160 zone: a ‘natural laboratory’ for crystal plastic deformation of quartz over a
 1161 temperature range from 250 to 700 C. *Journal of Structural Geology*, 24, 1861-

- 1162 1884. [https://doi.org/10.1016/S0191-8141\(02\)00035-4](https://doi.org/10.1016/S0191-8141(02)00035-4)
1163
- 1164 Stipp, M., Stünitz, H., Heilbronner, R., Schmid, S.M., 2002b. Dynamic recrystallization
1165 of quartz: correlation between natural and experimental conditions. In: De Meer,
1166 S., Drury, M.R., De Bresser, J.H.P., Pennock, G.M. (Eds.), *Deformation*
1167 *Mechanisms, Rheology and Tectonics: Current Status and Future Perspectives.*
1168 Geological Society, London, Special Publications, 200, 171 – 190.
1169 <https://doi.org/10.1144/GSL.SP.2001.200.01.11>
1170
- 1171 Stipp M., and Kunze, K., 2008. Dynamic recrystallization near the brittle- plastic
1172 transition in naturally and experimentally deformed quartz aggregates.
1173 *Tectonophysics*, 448, 77–97. <https://doi.org/10.1016/j.tecto.2007.11.041>
1174
- 1175 Tikoff, B., Teyssier, C.T., 1994. Strain modeling of displacement-field partitioning in
1176 transpressional orogens. *Journal of Structural Geology*, 16, 1575-1588.
1177 [https://doi.org/10.1016/0191-8141\(94\)90034-5](https://doi.org/10.1016/0191-8141(94)90034-5)
1178
- 1179 Toy, V.G., Prior, D.J., Norris, R.J., 2008. Quartz fabrics in the Alpine Fault mylonites:
1180 Influence of pre-existing preferred orientations on fabric development during
1181 progressive uplift. *Journal of Structural Geology*, 30, 602-
1182 621. <https://doi.org/10.1016/j.jsg.2008.01.001>
1183
- 1184 Trompette, R., 2000. Gondwana evolution; its assembly at around 600Ma. *Comptes*
1185 *Rendus de l'Académie des Sciences. Sciences de la terre et des planètes*, 330,
1186 305-315. [https://doi.org/10.1016/S1251-8050\(00\)00125-7](https://doi.org/10.1016/S1251-8050(00)00125-7)
1187
- 1188 Vernooij, M.G.C., den Brok, B., Kunze, K., 2006. Development of crystallographic
1189 preferred orientations by nucleation and growth of new grains in experimentally
1190 deformed quartz single crystals. *Tectonophysics*, 427, 35-53.
1191 <https://doi.org/10.1016/j.tecto.2006.06.008>
1192
- 1193 Wenk, H-R., Janssen, C., Kenkmann, T., Dresen, D., 2011. Mechanical twinning in
1194 quartz: Shock experiments, impact, pseudotachylites and fault breccias.
1195 *Tectonophysics* 510, 69-79. <https://doi.org/10.1016/j.tecto.2011.06.016>
1196
- 1197 Wheeler, J., Prior, D.J., Jiang, Z., Spiess, R., Trimby, P.W., 2001. The petrological
1198 significance of misorientations between grains. *Contributions to Mineralogy and*
1199 *Petrology*, 141, 109-124. <https://doi.org/10.1007/s004100000225>